

1 **Beyond excitation/inhibition imbalance in multidimensional models of neural circuit**  
2 **changes in brain disorders**

3 Cian O'Donnell<sup>1,2,\*</sup>, J. Tiago Gonçalves<sup>3,4</sup>, Carlos Portera-Cailliau<sup>3</sup> and Terrence J.  
4 Sejnowski<sup>2,5,\*</sup>

5 <sup>1</sup>Department of Computer Science, University of Bristol, Bristol, UK

6 <sup>2</sup>Howard Hughes Medical Institute, Salk Institute for Biological Studies, La Jolla CA, USA

7 <sup>3</sup>Departments of Neurology and Neurobiology, David Geffen School of Medicine at UCLA, Los  
8 Angeles, CA, USA

9 <sup>4</sup>Dominick Purpura Department of Neuroscience, Albert Einstein College of Medicine, Bronx,  
10 NY, USA

11 <sup>5</sup>Division of Biological Sciences, University of California at San Diego, La Jolla, CA, USA

12 \*Correspondence: cian.odonnell@bristol.ac.uk (C.O'D.), terry@salk.edu (T.J.S.)

13 **Abstract**

14 A leading theory holds that neurodevelopmental brain disorders arise from imbalances in  
15 excitatory and inhibitory (E/I) brain circuitry. However, it is unclear whether this one-  
16 dimensional model is rich enough to capture the multiple neural circuit alterations  
17 underlying brain disorders. Here we combined computational simulations with analysis of *in*  
18 *vivo* 2-photon Ca<sup>2+</sup> imaging data from somatosensory cortex of *Fmr1* knock-out (KO) mice, a  
19 model of Fragile-X Syndrome, to test the E/I imbalance theory. We found that: 1) The E/I  
20 imbalance model cannot account for joint alterations in the observed neural firing rates and  
21 correlations; 2) Neural circuit function is vastly more sensitive to changes in some cellular  
22 components over others; 3) The direction of circuit alterations in *Fmr1* KO mice changes  
23 across development. These findings suggest that the basic E/I imbalance model should be  
24 updated to higher-dimensional models that can better capture the multidimensional  
25 computational functions of neural circuits.

## 26 Introduction

27 The nervous system shows complex organization at many spatial scales: from genes and  
28 molecules, to cells and synapses, to neural circuits. Ultimately, the electrical and chemical  
29 signaling at all of these levels must give rise to the behavioral and cognitive processes seen at  
30 the whole-organism level. When trying to understand prevalent brain disorders such as autism  
31 and schizophrenia, a natural question to ask is: where is the most productive level of  
32 neuroscientific investigation? Traditionally, most major disorders are diagnosed entirely at the  
33 behavioral level, whereas pharmaceutical interventions are targeted at correcting alterations at  
34 the molecular level. However even for the most successful drugs, we have little understanding  
35 of how pharmaceutical actions at the molecular level percolate up the organizational ladder to  
36 affect behavior and cognition. This classic bottom-up approach may even be further  
37 confounded if phenotypic heterogeneity in disorders such as autism turn out not to reflect a  
38 unique cellular pathology, but rather “a perturbation of the network properties that emerge  
39 when neurons interact” (Belmonte et al., 2004). These considerations imply that a more  
40 promising level of analysis might be at the level of neural circuits, since the explanatory gap  
41 between circuits and behavior is smaller than the gap between molecules and behavior. This  
42 circuit-level viewpoint argues for a reverse-engineering approach to tackling brain disorders:  
43 rather than start at the molecular level and working up, we should instead start by asking how  
44 cognitive and behavioral symptoms manifest as alterations at the circuit level, then interpret  
45 these changes at the levels of cells, synapses, and molecules as appropriate.

46 One prominent circuit-level hypothesis for brain disorders has been the idea of an imbalance in  
47 excitatory and inhibitory signaling. First proposed as a model for autism (Rubenstein and  
48 Merzenich, 2003), the concept has since been applied to many other brain disorders, including  
49 Schizophrenia, Rett syndrome, fragile-X syndrome, tuberous sclerosis, and Angelman  
50 Syndrome. However, a major drawback of this model is that it only considers overall activity,  
51 which is 1-dimensional. It implies that either too much excitation or too much inhibition is  
52 unhealthy (Figure 1A). Although several studies have found evidence that the E/I balance is  
53 indeed upset in multiple brain disorders (Bateup et al., 2011; Dani et al., 2005; Gibson et al.,  
54 2008; Kehrer et al., 2008; Wallace et al., 2012), a model’s usefulness should not be judged on

55 whether it is nominally true or false, but on its explanatory and predictive powers as compared  
56 with competing alternative models. In this study we argue that that even if the E/I imbalance  
57 model proves correct, its unidimensionality might ultimately limit its applicability, for three  
58 reasons.

59 First, by placing all disorders on the same single axis, the E/I imbalance model implicitly lumps  
60 together some vastly different disorders, such as epilepsy, schizophrenia and autism (Figure  
61 1A) because they share an excess of excitation. By extension it implies that the symptoms of  
62 diverse disorders could be normalized solely by either enhancing or reducing the level of, say,  
63 GABAergic signaling as appropriate. Although clinical trials for such GABAergic-based  
64 interventions are ongoing (Braat and Kooy, 2015), no treatment for a neurodevelopmental  
65 disorder based on this principle has yet been approved.

66 A second issue with the unidimensionality of the E/I imbalance model is that it lumps together  
67 all excitatory and inhibitory neural circuit components. In Figure 1B we show a schematic  
68 diagram of a generic neural circuit with excitatory components colored red and inhibitory  
69 components colored blue. The E/I imbalance model implies that varying any of the excitatory  
70 components, such as the strength of recurrent excitatory synapses or the input resistances of  
71 excitatory neurons, would have the same overall effect on circuit function. In contrast, theorists  
72 have found that these equivalences often do not hold even in very simple circuit models  
73 (Wilson and Cowan, 1972).

74 Third, because the standard E/I imbalance model is given in terms of circuit components, not  
75 circuit function, it does not specify which aspect of a neural circuit's activity should be  
76 maintained for healthy performance. For example, it leaves unclear which of neuronal firing  
77 rates, synchrony, or reliability of responses might be altered if E/I balance is upset.

78 To motivate our study, we began by investigating which circuit activity properties are altered in  
79 a model brain disorder. We re-analyzed published *in vivo* 2-photon  $\text{Ca}^{2+}$  imaging data we  
80 previously recorded from somatosensory cortex in *Fmr1* knockout mice (Gonçalves et al.,  
81 2013), a well-studied animal model for fragile-X syndrome (The Dutch-Belgian Fragile X  
82 Consortium, 1994). We compared the data from wild-type (WT) mice with *Fmr1* KO mice,

83 across three different developmental time points: just before (P9–11) and after (P14–16) the  
 84 critical period for heightened activity-dependent synaptic plasticity in L2/3 barrel cortex, and a  
 85 more mature timepoint (P30–40). Example  $\Delta F/F$  raster plots from each group are shown in  
 86 Figure 1C, top left. We binned the data into 1 s timebins (originally imaged at 4 Hz), then  
 87 transformed each neuron's timeseries of  $\Delta F/F$  values into a probabilistic sequence of binary  
 88 ON/OFF values by assuming a Poisson firing model (Methods). We then summarized the  
 89 neural population activity from each animal with three statistics: the mean ON probability  
 90 across all recorded neurons, the standard deviation (s.d.) in ON probability across neurons,  
 91 and the mean correlation between all pairs of neurons (Figure 1C, bar charts right and scatter  
 92 plots lower left). Together these measures capture both the statistics of the bulk population  
 93 activity and some indication of the heterogeneity across neurons.

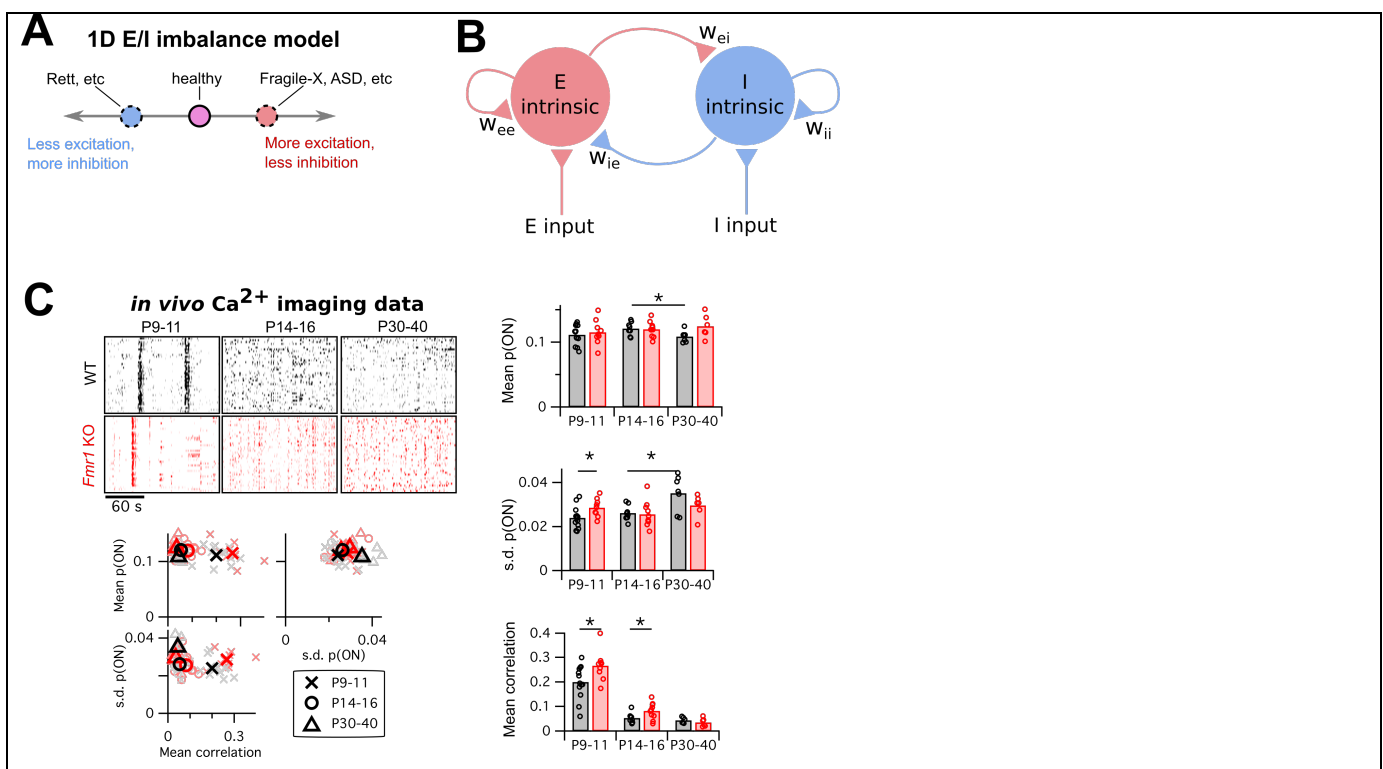


**Figure 1. Mismatch between the E/I imbalance model's unidimensionality and the multiple changes in circuit activity in Fragile-X mouse models.**

**A:** Schematic of standard E/I imbalance model as a unidimensional axis.

**B:** Diagram of a generic neural circuit, showing an excitatory and an inhibitory population of neurons and their interconnections. Although the E/I imbalance model implicitly groups all

components as either excitatory (red) or inhibitory (blue), in principle any component could separately be altered in brain disorders, and may have a distinct effect on circuit function.

**C:** Upper left, example  $\text{Ca}^{2+}$  imaging dF/F raster plots from a single animal from each of two genotypes, WT and *Fmr1* KO, and three age groups, P9–11, P14–16 and P30–40. In each case 3 minutes of data are shown from 40 neurons. Right and lower left, mean firing probability, standard deviation of firing probabilities, and mean pairwise correlation across all neurons. Same data in scatter plots lower left and bar charts right. \* indicates significant difference in group means at  $p < 0.05$ , by bootstrapping.

94 For mean firing rates, the only change we detected was a decrease in firing probability in WT  
95 between P14–16 and P30–40 ( $p = 0.027$ ), which was coupled with an increased s.d. of firing  
96 rates ( $p = 0.015$ ). We also detected a higher firing rate s.d. in P9–11 KO animals than WT ( $p =$   
97  $0.031$ ). Finally, as previously reported (Golshani et al., 2009; Gonçalves et al., 2013; Rochefort  
98 et al., 2009), we found a substantial decrease in pairwise correlations in both genotypes  
99 across development, with slightly higher correlations in KO animals than WT at P9–11 ( $p =$   
100  $0.029$ ) and P14–16 ( $p = 0.047$ ).

101 These results show that multiple statistics of cortical circuit activity are altered in *Fmr1* KO  
102 mice. However, two questions remain: 1) Which circuit components are responsible for these  
103 activity alterations? 2) What is the consequence for circuit computation? In the remainder of  
104 this study, we used computational simulations and further data analysis to ask whether the E/I  
105 imbalance model could help address these questions.

106 We first built a detailed spiking neural circuit model of mouse L2/3 somatosensory cortex to  
107 explore how its various excitatory and inhibitory components affect the circuit's spiking output,  
108 and found that the E/I imbalance model was not flexible enough to capture key aspects of this  
109 relationship. We then derived an abstract 2-dimensional circuit model that captures more  
110 features of the circuit function than the 1-dimensional E/I imbalance model did. Using this new  
111 model, we found that certain sets of circuit components have redundant effects on circuit  
112 function, and that circuit function is vastly more sensitive to changes in some components over  
113 others. To ask how this 2-D model could help interpret brain circuit abnormalities in a particular  
114 test case, we fit a version of the model to the  $\text{Ca}^{2+}$  imaging data from Fragile-X mouse models

115 presented above. We found that the model predicts opposite changes in *Fmr1* KO circuit  
116 properties at different developmental ages. Finally, we applied a new large-scale neural  
117 population analysis method (O'Donnell et al., 2017) to the same Ca<sup>2+</sup> imaging data, and found  
118 systematic shifts in the distribution of neural circuit activity patterns in Fragile-X that were not  
119 predictable from neural firing rates or correlations alone.

## 120 Results

121 Neural circuits consist of many components that typically interact non-linearly to generate  
122 complex circuit activity dynamics. Although many properties of cortical circuit components  
123 have been found to be altered in animal models of brain disorders, it remains extremely difficult  
124 to predict the net effect of varying any one particular parameter on circuit activity. The E/I  
125 imbalance model seeks to simplify this problem by projecting all circuit alterations onto a one-  
126 dimensional axis (Figure 1A) where the goal is to achieve a 'healthy' balance of excitation and  
127 inhibition. Under this model, either too much excitation or too much inhibition leads to improper  
128 circuit function.

129 To explicitly test whether the E/I imbalance model can account for the effects of cellular  
130 component changes on circuit function, we built a detailed computational model of layer (L) 2/3  
131 mouse somatosensory cortex. This circuit has been studied in detail by neurophysiologists,  
132 and several of its properties have been found to be altered during development in mouse  
133 models of Fragile-X syndrome, including parvalbumin-positive interneuron number (Selby et al.,  
134 2007), GABA receptor reversal potential (He et al., 2014), dendritic spine dynamics (Cruz-  
135 Martin et al., 2010), and L4 excitatory input (Bureau et al., 2008), reviewed by Contractor et al.  
136 (2015). We used numerical computer simulations to perform hypothetical experiments where  
137 we perturbed various parameters of the circuit model and observed the resulting changes in  
138 circuit-level activity. Although we focused on this particular brain circuit for tractability, our  
139 general conclusions and methodology should be readily applicable to other brain circuits (Frye  
140 and Maclean, 2016).

141 The L2/3 computational model we built (Figure 2A, see Methods for details) consisted of four  
142 interconnected populations of leaky integrate-and-fire neurons: one group of 1700 excitatory  
143 (E) pyramidal neurons and three groups of inhibitory neurons: 115 5HT<sub>3A</sub>R-expressing neurons,  
144 70 parvalbumin-expressing (PV) neurons, and 45 somatostatin-expressing (SOM) neurons.  
145 This L2/3 circuit was driven by a separate population of 1500 L4 excitatory neurons. Cellular  
146 numbers, intrinsic properties, synaptic strengths, and connectivity statistics were taken from  
147 published *in vitro* data from P17–22 wild-type mice (Avermann et al., 2012; Lefort et al., 2009;

148 Tomm et al., 2014). We chose this level of detail for the model in order to relate experimentally  
149 measureable biophysical properties of neurons to their putative role in the circuit at large.  
150 L2/3 neurons of the rodent somatosensory neocortex respond only sparsely to sensory  
151 stimulation *in vivo*. For example, twitching a whisker activates, on average, only ~20% of L2/3  
152 neurons in its corresponding barrel, each of which typically emits only one action potential  
153 (Clancy et al., 2015; Kerr et al., 2007; Sato et al., 2007). Hence any individual neuron carries  
154 very little information about the stimulus on its own, implying that information must instead be  
155 encoded at the circuit level as the identities of the subset of neurons that respond.

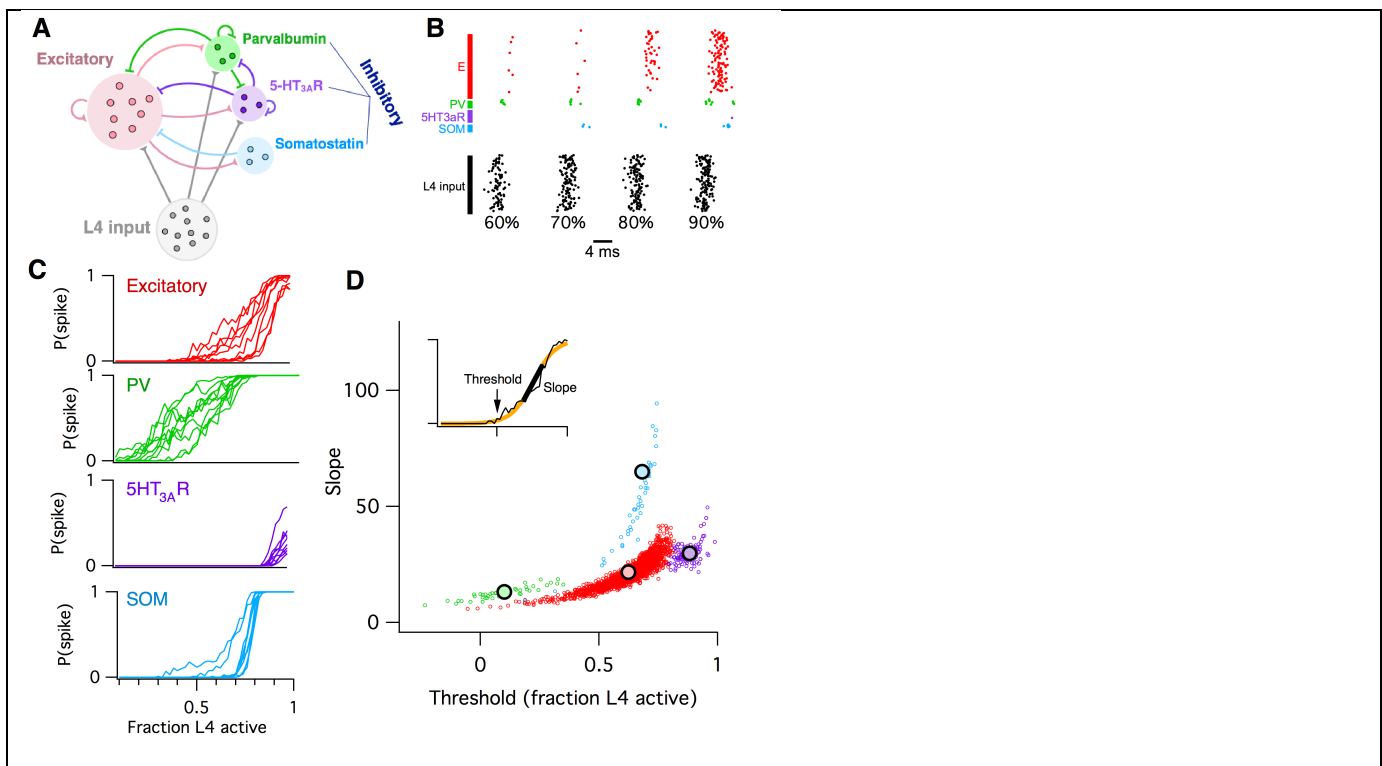


**Figure 2. Computational model of L2/3 mouse somatosensory cortex.**

**A:** Schematic diagram of computational circuit model.

**B:** Example raster plots of spiking responses from a subset of neurons from each cell type (colors as in panel A), for varying fractions of L4 activated (black).

**C:** Probability of spiking as a function of the fraction of L4 neurons activated. Each curve represents the response probability of a single neuron, averaged over multiple trials and multiple permutations of active L4 cells.



**D:** Each circle plots the fitted logistic slope and threshold values for a single neuron in the simulation. Circle color indicates cell type: red is excitatory, green is PV inhibitory, purple is 5HT<sub>3A</sub>R inhibitory, blue is SOM inhibitory. Large black circles indicate mean for each cell-type. Inset shows an example fitted logistic response function (orange) to the noisy simulation results from a single excitatory neuron (black).

156 To model whisker stimulation, we simulated a volley of spikes arriving from L4 as input to the  
157 population of L2/3 cells. We chose a random subset of L4 neurons as ON, then sent a single  
158 spike from each of these L4 cells to their target neurons in L2/3, and recorded the responses  
159 of all neurons in L2/3, some of which spiked and some of which did not. We repeated this  
160 identical stimulation multiple times, in order to get an average response probability for each  
161 L2/3 neuron, given the probabilistic vesicle release at synapses in the model. Then we chose a  
162 different random subset of L4 neurons as ON, and repeated the entire procedure. Finally, we  
163 varied the fraction of L4 cells active and plotted the probability of response for each individual  
164 L2/3 neuron as a function of L4 activity level (Figure 2B–C).

165 We found that the mean response probability of each neuron in the simulation increased from  
166 zero to one monotonically with increasing L4 activity level. This sigmoidal-shaped response  
167 profile of simulated L2/3 neurons mimics the spiking response of mouse L2/3 pyramidal cells to  
168 extracellular L4 stimulation *in vitro* (Elstrott et al., 2014), while the sparse, noisy and distributed  
169 network responses were reminiscent of *in vivo* activity following whisker stimulation (Clancy et  
170 al., 2015; Kerr et al., 2007). Neurons of all four cell types in the simulation responded to the L4  
171 stimulus, including the SOM interneurons which did not receive direct L4 input, but were  
172 instead activated by disynaptic connections via L2/3 excitatory neurons. The detailed shape of  
173 the response curve varied systematically across cell types, and was heterogeneous for  
174 different neurons of a given cell type. To quantify these differences, we used logistic  
175 regression to fit the response profile of each neuron with a sigmoid function (Figure 2D, inset),  
176 which has just two parameters: the slope (representing the steepness of the response curve)  
177 and threshold (representing the minimal fraction of L4 neurons needed to activate the cell).  
178 When we plotted the fitted slope and threshold values for each neuron against each other, we  
179 found that each cell type falls into a distinct cluster in this 2-dimensional space. For example,

180 all PV inhibitory neurons had a low slope and low threshold, whereas SOM inhibitory neurons  
181 had a steep slope and moderate threshold. We then used these slope-threshold  
182 measurements to summarize the circuit-level input-output function of this 'default' model of  
183 L2/3 somatosensory cortex. This 2-D logistic model has two benefits over the 1-D E/I  
184 imbalance model: first, its extra degree of freedom allows for richer and more flexible fits to  
185 data, and second, by describing an input-output mapping for the L2/3 circuit it can capture  
186 some aspects of the computation that the circuit performs for the animal. In contrast, the E/I  
187 imbalance model is specified purely in terms of circuit components, and so is agnostic to the  
188 circuit's computational function.

189 The biophysical circuit model contained 100 parameters (Methods). How sensitive is the  
190 circuit's macroscopic input-output function to alterations in its low-level components? To test  
191 this, we varied 76 of the model parameters in turn by  $\pm 20\%$ , and repeated the entire set of  
192 simulations for each case (Methods). For each individual parameter alteration, we fit a new  
193 logistic response function for each model neuron. We summarize the results by plotting the  
194 logistic slope and threshold parameters and comparing their values to those found with the  
195 default model. The outcomes were hugely varied. We show three examples from the set of  
196 seventy-six in Figure 3A, chosen to illustrate three qualitatively different effects that neural  
197 parameter changes can have on circuit function. First, when we increased the amplitude of  
198 postsynaptic potentials (PSPs) of excitatory synapses from L4 to L2/3 excitatory neurons, we  
199 found that the logistic threshold parameter of all cell types shifted leftwards to lower values  
200 (Figure 3A left), implying that fewer L4 neurons were needed to activate the entire L2/3 circuit.  
201 In contrast, when we increased the PSP amplitude of a different excitatory synapse, the  
202 recurrent connections between L2/3 excitatory neurons, we found (Figure 3A center) that  
203 excitatory and SOM inhibitory neurons had increased slope parameters relative to default, with  
204 little change in their threshold parameters. 5HT<sub>3A</sub>R inhibitory neurons had decreased slopes  
205 and thresholds, while PV neurons had little change at all. As a third example we increased the  
206 probability of inhibitory synaptic connections from L2/3 PV interneurons to L2/3 excitatory  
207 neurons (Figure 3A right). In this case we found that excitatory neurons had a lower slope and  
208 increased threshold, SOM inhibitory neurons had a lower slope, 5HT<sub>3A</sub>R inhibitory neurons had

209 both an increased slope and threshold, and PV neurons showed little change, even though  
 210 their outgoing synapses were the parameter that was altered.

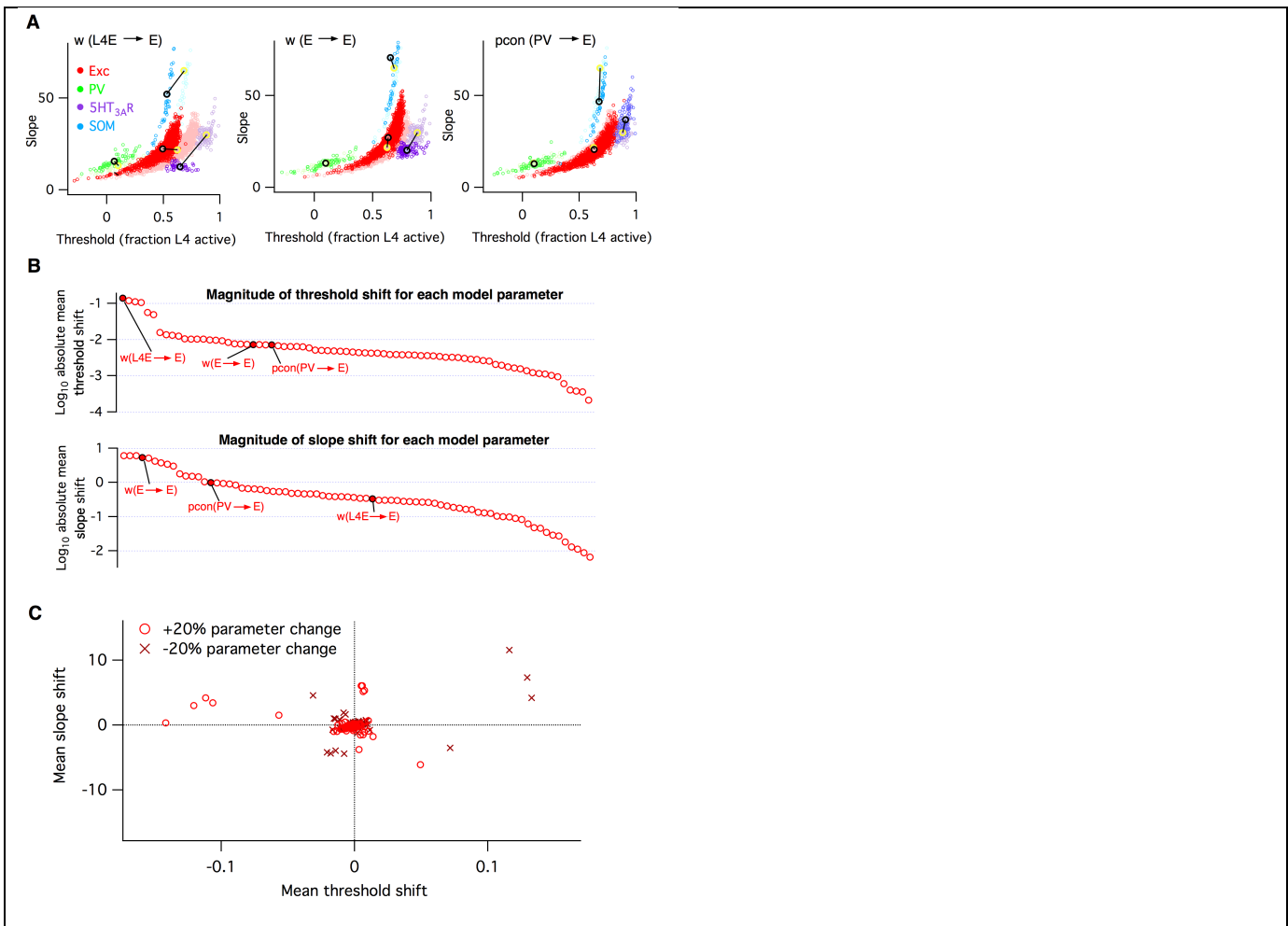


**Figure 3. Heterogeneous effects of varying L2/3 parameters on the circuit input-output function.**

**A:** Shifts in the distribution of fitted slope and threshold parameters as a result of increasing the strength of synapses from L4 to L2/3 E neurons (left), increasing the strength of recurrent synapses between L2/3 E neurons (center), or increasing the connection probability between L2/3 PV interneurons and E neurons (right). Transparent circles represent values for default network, heavy circles for altered network. The default and altered group means are large yellow and black open circles, respectively.

**B:** Absolute values of mean shifts in threshold (upper plot) and slope (lower plot) for Excitatory neurons arising from increasing the value of each parameter by +20%. The three example

parameters from panel A are labeled and indicated as filled red circles. Note that data are presented on a log<sub>10</sub> scale.

**C:** The shift in mean slope-threshold parameter values for E neurons from the default network values, in response to each of the 76 circuit parameter alterations. Light red circles indicate +20% increase in parameter value; dark red crosses indicate a -20% decrease in parameter value.

211 To synthesize the findings from all simulations, for each altered parameter we plotted the shift  
212 in mean slope-threshold values for L2/3 excitatory neurons from the mean values found with  
213 the default model (Figure 3B). We focused on excitatory neurons because they constitute 90%  
214 of the neurons in this layer (Lefort et al., 2009) and are the primary output to downstream  
215 circuits (Mao et al., 2011; Petreanu et al., 2007). Overall, we found a very heterogeneous  
216 picture. First, the magnitude of the shift in circuit response varied from parameter to parameter  
217 (Figure 3B—C). Varying some parameters, such as the first two examples given above, had  
218 large effects, whereas varying other parameters such as  $w_{15htE}$  (the strength of synapses from  
219 5HT<sub>3A</sub>R inhibitory neurons to E neurons) or  $\tau m_{Isom}$  (the membrane time constant of SOM  
220 inhibitory neurons) had little effect. Second, the direction of shift in 2-D slope-threshold space  
221 also depended on parameter (Figure 3C). Increasing some parameters changed either circuit  
222 slope or threshold in isolation, while other parameters changed both slope and threshold  
223 together. All four quadrants of the slope-threshold plane could be reached by various subsets  
224 of the model parameters. Third, basic knowledge of whether a component was ‘excitatory’ or  
225 ‘inhibitory’ was insufficient to predict the direction of slope-threshold change. For example, the  
226 two glutamatergic projections considered in Figure 3A had distinct effects on circuit function.

227 In summary, these simulations indicate that the L2/3 somatosensory cortex circuit has  
228 extremely varied sensitivities to changes in its cellular components, and that the eventual  
229 circuit-level consequences cannot be predicted from knowledge of the class of the perturbed  
230 neurotransmitter alone. Since the E/I imbalance model groups all excitatory and inhibitory  
231 components as respective equals, it cannot account for these results.

232 ***Firing rates and correlations from the logistic model***

233 In the above analysis, we investigated how low-level circuit components affect a high-level  
234 circuit input-output function, as parameterized by the slope and threshold of fitted logistic  
235 functions. But how is this logistic input-output function related to more common measures of  
236 neural population activity, such as firing rates and pairwise correlations between neurons? To  
237 investigate this, we considered the following reduced statistical model of cortical activity. We  
238 assumed for simplicity that the magnitude of the total input to the L2/3 circuit can be described  
239 by a Gaussian distributed random variable, with zero mean and unit standard deviation (Figure  
240 4A lower left). Then we described each L2/3 neuron's input-output as a logistic function as  
241 before (Figure 4A upper left), with threshold and slope defined relative to the Gaussian input's  
242 mean and standard deviation, respectively. Given this model, we can numerically calculate the  
243 probability distribution over a neuron's firing probability, which in general is skewed and non-  
244 Gaussian (Figure 4A upper right). From this function we compute (Methods) both the neuron's  
245 mean firing probability and the pairwise correlation of two identical neurons following this  
246 profile (Figure 4A lower right). Example samples from the model are illustrated in Figure 4B.

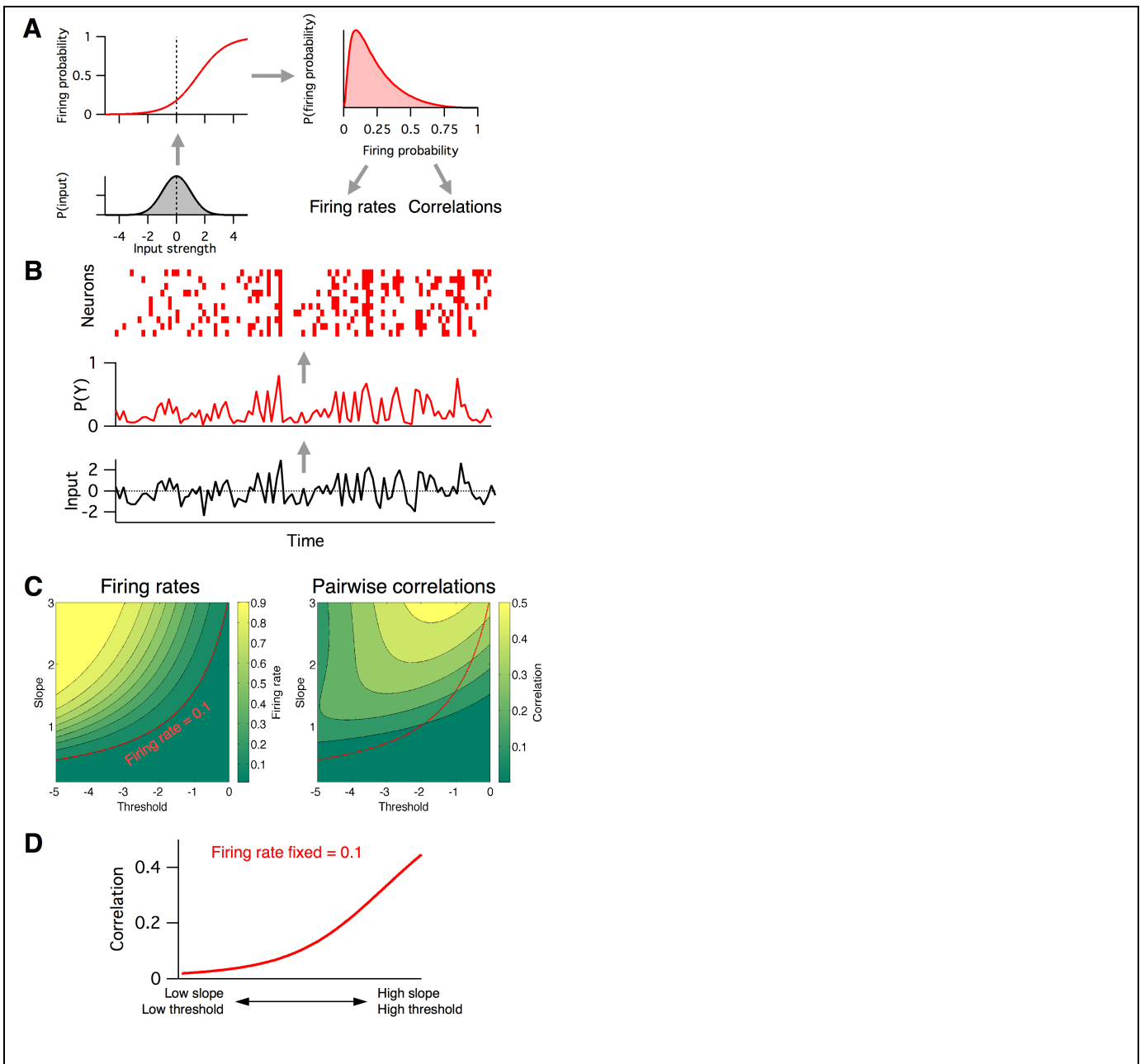


**Figure 4. Firing rates and pairwise correlations from the logistic response model.**

**A:** Logistic model components. We assume a normally distributed input drive (gray distribution, bottom left), which is passed through the neuron's probabilistic spike input-output function (red curve, top left), which results in a distribution of spike probabilities (top right) that are determined by the input-output function's slope and threshold parameters. From the output distribution we can directly calculate the mean firing rate and correlation between a pair of such neurons (Methods).

**B:** Example spikes from the logistic model. The bottom trace (black) shows examples inputs over time drawn randomly from the same normal distribution. This is transformed to spike probability at each time point (red trace). Example spike trains can then be generated from the spike probability trace by drawing Bernoulli samples with the specified probabilities (red ticks, top). If each neuron's spike train is conditionally independent given the same spike probabilities, we can see correlations in their spike trains.

**C:** Calculated mean firing rate (left) and pairwise correlation (right) color maps as a function of the logistic threshold (x-axis) and slope (y-axis) parameters. Contours indicate lines of fixed firing rate or correlation in the 2D slope-threshold space.

**D:** Pairwise correlation values along the slope-threshold contour for firing rate = 0.1.

247 Neural firing rates and correlations had qualitatively different dependencies on the underlying  
248 logistic model's slope and threshold. Neural firing rate was greatest when threshold was low  
249 and slope was high (top left of phase plot, Figure 4C left), whereas correlations were greatest  
250 when both threshold and slope were high (top right of phase plot, Figure 4C right). This implies  
251 that any change in the circuit's input-output function slope or threshold will in general have  
252 distinct effects on firing rate versus correlations, and so could not be captured by a 1-  
253 dimensional E/I balance model that sought to for example normalize firing rates alone. To  
254 illustrate this fact, we plot the calculated correlation values along a contour where firing  
255 probability is fixed at 0.1 (Figure 4D). In the region of parameter space where both the slope  
256 and threshold are low (Figure 4C bottom left), correlations are low,  $\sim 0.01$ . However, as we  
257 move along the contour for firing rate = 0.1 towards the region of parameter space where slope  
258 and threshold are high (Figure 4C top right), the pairwise correlations increase to  $\sim 0.4$ . This  
259 shows that a 1-dimensional E/I balance rule that exclusively sought to normalize neural firing  
260 rates would leave neural correlations free to achieve arbitrary values.

261 Previous studies have found evidence for an E/I imbalance in ASD (Lee et al., 2017; Nelson  
262 and Valakh, 2015). Fragile-X syndrome is the leading inherited cause of ASD, and also carries  
263 alterations in excitability (Contractor et al., 2015). We aimed to interpret our *Fmr1* KO  $Ca^{2+}$   
264 imaging data (Figure 1C) via the 2D logistic model. Since our earlier analysis found important  
265 differences in the heterogeneity in firing rates across neurons in *Fmr1* KOs (Figure 1C), we

266 extended the 2-D logistic model for single neurons to a 5-D neural population version that  
267 captured cell-to-cell heterogeneity. The three extra parameters represented the standard  
268 deviations and correlation in slope and threshold parameters across the neural population (see  
269 Methods for details). We fit the parameters of the logistic model to reproduce the same neural  
270 population  $\text{Ca}^{2+}$  imaging data presented in Figure 1C. Given the three summary statistics from  
271 each animal (firing rate mean and s.d., and mean pairwise correlation), we used a gradient  
272 descent algorithm to find the five parameters of the population-level version of the logistic  
273 model that best matched the activity statistics (see Methods). The output statistics of the fitted  
274 models matched well that of the target data (Figure 5 – figure supplement 1). Example neural  
275 population activity patterns drawn from the mean model fits for each group are shown in Figure  
276 5A, along with the fitted slope-threshold functions (Figure 5A insets), to be compared with the  
277  $\text{Ca}^{2+}$  imaging rasters in Figure 1C. For each animal, we also plot the full 5-D parameter fits for  
278 all animals in Figure 5 – figure supplement 2. For the rest of the analysis, we focus on the  
279 mean slope and mean threshold parameters, which showed the most prominent changes.  
280 However we also note an increase in the slope s.d. between P14-16 and P30-40 WT animals  
281 that was not observed in *Fmr1* KO, mirroring the increased heterogeneity in firing rates in the  
282 same animals (Figure 1C). In Figure 5B we plot the mean slope and mean threshold fits on top  
283 of the previously calculated (Figure 4C) 2D slope-threshold maps of firing rate and correlation.  
284 We found that in young animals, P9–11, most points were scattered at high values of both  
285 slope and threshold (Figure 5B left). With age, the parameter fits for both genotypes moved  
286 south-west towards the low slope and low threshold region of parameter space (Figure 5B  
287 center and right). The mean location of the cloud of points at each developmental age differed  
288 between WT and KO. We plot the direction of shift in group mean from WT to KO in Figure 5C.  
289 In young animals, P9–11 and P14–16, the KO group had both higher slope and higher  
290 threshold than WT, whereas in adult animals, P30–40, the KO group had a lower slope and  
291 lower threshold than WT. These results demonstrate an opposite direction of circuit parameter  
292 change in young Fragile-X mice compared to adults, which was not be uncovered by  
293 measures of neural firing rates and correlations (Figure 1C).



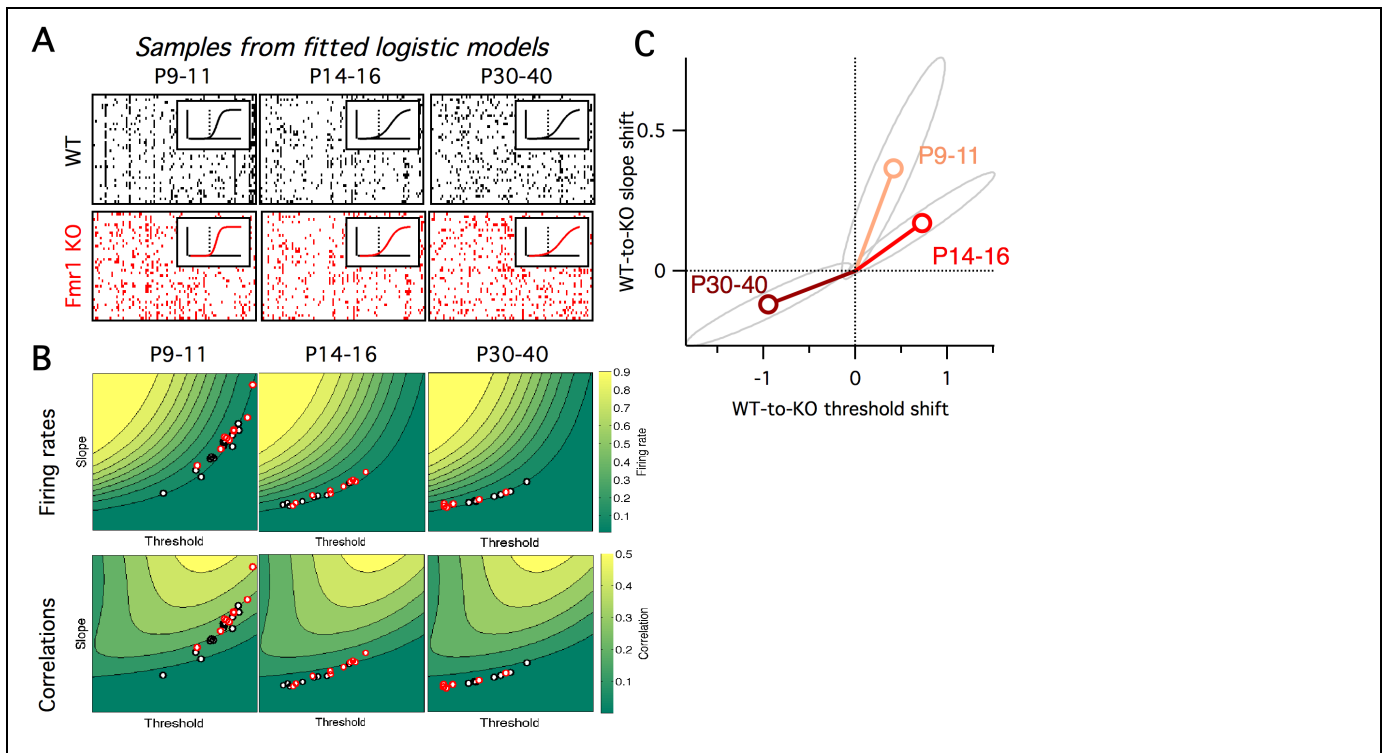


**Figure 5. Fragile-X fits from logistic model.**

**A:** Example samples from the fitted logistic models, corresponding to the six groups shown in panel A. Inset shows group mean fitted logistic function, dashed vertical line represents zero.

**B:** Fitted logistic mean slope and mean threshold values for data from each WT (black circles) and *Fmr1* KO (red circles) animal. Values overlaid on same firing rate (top) and correlation (bottom) maps from Figure 4C.

**C:** Shift in mean logistic slope and threshold values from WT to KO for P9–11 (orange), P14–16 (red) and P30–40 (brown). Grey ellipses represent 95% confidence intervals (Methods).

294 Earlier we asked how sensitive the logistic model slope and threshold parameters were to  
295 alterations in the many underlying neural circuit components (Figure 3). In a similar way, we  
296 can also ask how sensitive the neural firing rates and correlations are to alterations in the  
297 logistic slope and threshold parameters. This is important since inspection of the 2-dimensional  
298 maps in Figure 3C shows that these sensitivities will differ depending on starting location within  
299 the slope-threshold space. To quantify this effect, we calculated the sensitivity of both the firing  
300 rate and correlations to small changes in the slope and threshold (Figure 6A-B, see Methods),  
301 quantified as the partial derivatives local to the fitted logistic parameter values for each animal

302 (black and red circles in Figure 5B). In general, increasing the slope or decreasing the  
303 threshold always increased both firing rates and correlations, as can be predicted from Figure  
304 5B. However, the magnitude of sensitivities varied across animals. We found only minor  
305 differences in sensitivities between genotypes (Figure 5 – figure supplement 2), and as a result  
306 we pooled the sensitivity measurements across genotypes to test for statistical differences in  
307 sensitivity with developmental age. In young animals, P9–11, changes in the logistic threshold  
308 (solid bars in Figure 6) had substantial effects on both firing rates and correlation. This  
309 sensitivity decreased with age ( $p \leq 0.013$  for firing rates,  $p < 0.01$  for correlations from P9–11  
310 to P14–16), so that in adult animals, P30-40, changes in threshold had relatively little effect  
311 on neural activity statistics. A different picture emerged for the logistic slope parameter (striped  
312 bars in Figure 6). There, the firing rate sensitivity increased with from P9–11 to P14–16 ( $p <$   
313  $1e-6$ ) (Figure 6A), while correlation sensitivity stayed approximately constant ( $p \geq 0.18$ ) (Figure  
314 6B). These results show that the quantitative relationships between neural activity statistics  
315 and the underlying circuit parameters are not fixed across development.

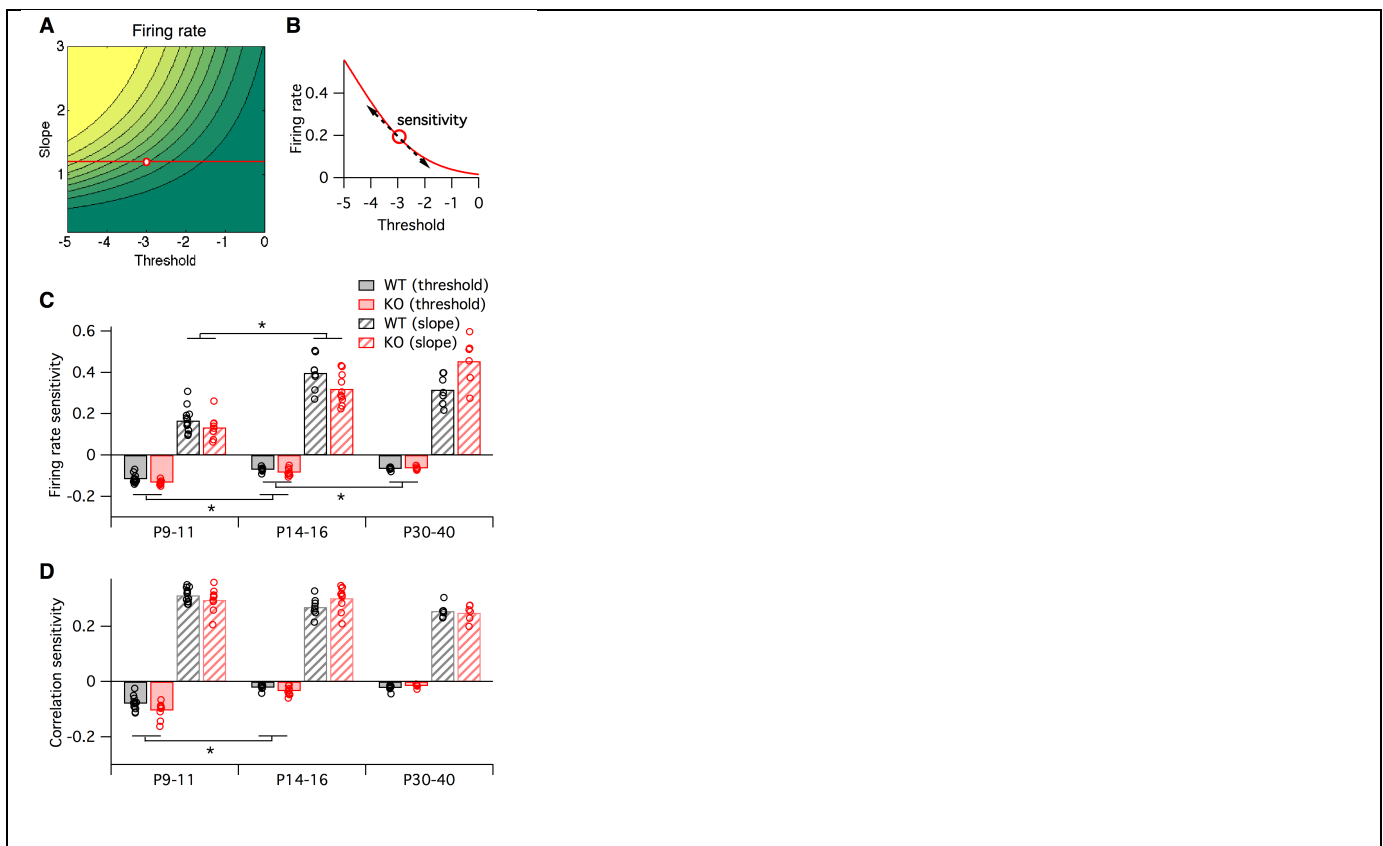


**Figure 6. Sensitivity of firing rate and correlations with respect to logistic model parameters, local to the parameter fit for each animal.**

**A-B:** Sensitivity to a parameter is calculated about a given point in parameter space. In this hypothetical example, we plot a slope-threshold parameter fit at the red circle on the firing rate contour map (A). The firing rate varies non-linearly if the threshold is varied away from this point (B). Sensitivity is calculated as the local derivative, or slope of the tangent, about the target point.

**C-D:** Sensitivity of firing probability (C) and pairwise correlations (D) to change in threshold (solid bars) and slope (striped bars) parameters of logistic model, about the fitted parameter values for each animal (circles) displayed in Figure 5B. Bars represent group means. Each statistical test compares the mean values between adjacent pairs of age groups, where the data were pooled between genotypes.

316 What are the functional implications of these alterations in firing rates and correlations in  
317 Fragile-X mice across development? To address this, we calculated the entropy of the neural  
318 population activity for the data from each animal. Entropy is a quantity from information theory,  
319 measured in bits, that puts a hard upper bound on the amount of information that can be  
320 represented by any coding system (Cover and Thomas, 2006). Intuitively, the entropy  
321 measures how uniform the neural population activity pattern distribution is: it is large if the  
322 circuit exhibits many different activity patterns over time, and small if only a few activity  
323 patterns dominate. Entropy is an appealing measure for the present problem because it is  
324 sensitive both to neural firing rates and to correlations at all orders. It is typically highest when  
325 firing rates are high and correlations are low. Although entropy is notoriously difficult to  
326 calculate for large neural populations because most estimation methods require impractically  
327 long data recordings (Quiñ Quiroga and Panzeri, 2009), we recently developed a new  
328 statistical method for this purpose, called the *population tracking model*, that scales well to  
329 large numbers of neurons, even for limited data (O'Donnell et al., 2017). This model matches  
330 both the synchrony distribution for the number of neurons simultaneously active, and the  
331 variations in individual cell-to-cell firing rates. We fit this population tracking model to the same  
332 Ca<sup>2+</sup> imaging data as analyzed above (Figure 7). An intermediate step in estimating the neural  
333 entropy involves calculating a low-parameter approximation of the entire probability distribution

334 over all  $2^N$  neural population activity patterns, where  $N$  is the number of neurons. The  
335 cumulatives of these probability distributions calculated for 50-neuron subsets of the  
336 recordings are shown in Figure 7A. In young animals P9–11, a small number of activity  
337 patterns accounts for a large fraction of the probability mass (Figure 7A left). For example,  
338 based on these curves, 50% of the time we would expect to see the same 1000–10,000  
339 patterns out of a possible total  $2^{50} \approx 10^{15}$  patterns. In contrast, in older animals P14–16 and  
340 P30–40 the cumulative distributions shift rightwards so that more patterns are typically  
341 observed (Figure 7A center, right). In these cases, around 1,000,000 patterns are needed to  
342 account for 50% probability mass.

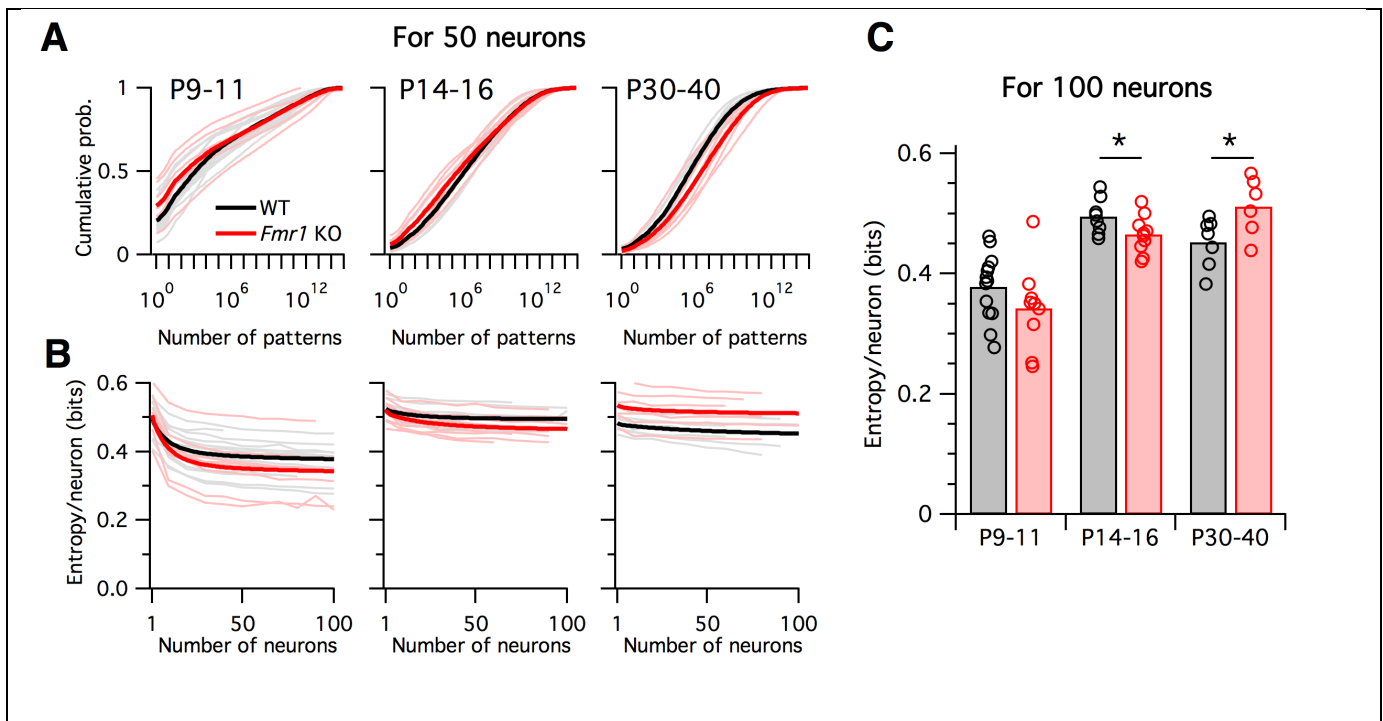


**Figure 7. Differing trajectories of WT and KO entropy across development.**

**A:** Cumulative probability mass as a function of the number of patterns. Patterns ordered from most probable to least probable. Thin lines are mean across many randomly-chosen 50-neuron subsets from a given animal, and thick lines represent means across all animals of a given genotype.

**B:** Entropy per neuron as a function of the number of neurons analyzed. Thin lines are mean across many randomly chosen subsets for a given animal, thick lines are group mean of

double exponential fits to the data (see Methods). Age groups (left to right) are as in panel A. **C:** Estimated entropy/neuron for 100 neuron populations. Circles represent individual animals, bars are group means.

343

344 Instead of attempting to quantify these shifts by asking how many patterns are needed to cross  
345 an arbitrary threshold of probability mass, we instead calculated the entropy, which takes into  
346 account the shape of the entire probability distribution. The entropy depends on the number of  
347 neurons analyzed, so we normalized all estimates to calculate the entropy per neuron (Figure  
348 7B—C). Since we are treating neurons as binary, the entropy/neuron was bounded between 0  
349 and 1 bits. For all age groups, and for both WT and *Fmr1* KO animals, entropy/neuron  
350 progressively decreased with the number of neurons analyzed (Figure 7B). Because each  
351 imaging session captured a different number of neurons (range 40—198, median 97), we fit  
352 the entropy/neuron versus number of neurons data with a double exponential function (see  
353 Methods) and use the fit to provide a standardized estimate of the entropy/neuron for 100-  
354 neuron populations (Figure 7C). In WT animals, entropy/neuron showed a non-monotonic  
355 trajectory across development (O'Donnell et al., 2017). At P9—11 it was low, 0.38 bits (95% c.i.  
356 [0.35:0.41]), before increasing at P14—16 ( $p < 0.001$ ) to 0.50 bits (95% c.i. [0.48:0.52]), before  
357 decreasing again at P30—40 ( $p = 0.028$ ) to 0.45 bits (95% c.i. [0.42:0.48]). We found a  
358 different entropy trajectory in *Fmr1* KO animals. There, although entropy/neuron also began  
359 low at 0.34 bits (95% c.i. [0.30:0.39]), not different from WT ( $p = 0.19$ ), when it increased at  
360 P14—16 ( $p < 0.001$ ) to 0.465 bits (95% c.i. [0.45:0.48]) it remained lower than for WT ( $p =$   
361 0.048). Finally, instead of decreasing as in the WT case, entropy continued to increase in  
362 P30—40 *Fmr1* KO animals ( $p = 0.033$ ) to 0.51 bits (95% c.i. [0.47:0.55]), higher than WT ( $p =$   
363 0.034). These entropy values estimated directly from  $\text{Ca}^{2+}$  imaging data agreed well with  
364 entropy estimates for synthetic data sampled from the previously fit logistic models (Figure 7 –  
365 figure supplement 1). In summary, unlike WT animals, *Fmr1* KO mice showed a monotonically  
366 increasing entropy/neuron from P9—11 to P30—40. Furthermore, the direction of change in  
367 entropy between P14—16 and P30—40 was opposite for WT and *Fmr1* KO animals,  
368 decreasing in the former and increasing in the latter.

## 369 Discussion

370 The 1-dimensional E/I imbalance model has been widely used for interpreting neural circuit  
371 changes observed in animal models of diverse brain disorders (Bateup et al., 2011; Dani et al.,  
372 2005; Gibson et al., 2008; Kehrer et al., 2008; Wallace et al., 2012). In the case of Fragile-X  
373 syndrome, the hyperexcitability prediction of the E/I imbalance model is consistent with many  
374 of the symptoms of the disease (e.g. seizures, hyperarousal, hyperactivity, hypersensitivity to  
375 sensory stimuli) and the known pathogenic defects implicated in *Fmr1* KO mice (diminished  
376 GABA signaling, exaggerated intrinsic excitability, increased neuronal firing rates; reviewed by  
377 Contractor et al., 2015). Here we tested the hypothesis that the E/I imbalance model can  
378 account for alterations in other neural activity statistics beyond the mean firing rates; however,  
379 our results demonstrated that it was inadequate. The model was too inflexible to account for  
380 the joint alterations in both neural firing rates and correlations observed in Fragile-X model  
381 mice. This suggests that future studies of brain disorders may need to consider higher-  
382 dimensional models of neural circuit dysfunction.

383 To test how cellular components affect their circuit function, we built computational models of  
384 mouse L2/3 somatosensory cortex at two levels of abstraction: a detailed, 100-parameter  
385 biophysical model, and a 2-parameter logistic response model. The purpose of the detailed  
386 model was to build a representation of the circuit where each parameter has a one-to-one  
387 mapping with something that could be experimentally measured in a real animal - indeed many  
388 of these parameters have been shown to be altered in *Fmr1* KO mice. The purpose of the  
389 logistic model was different: it simple enough to be both derivable from the complex model,  
390 and provide a direct link with measurable activity variables in our *in vivo* Ca<sup>2+</sup> imaging data,  
391 firing rates and correlations. The disadvantages of detailed models are that they contain many  
392 parameters, and so are hard to constrain to data – in this case it was only possible because of  
393 the large dataset from Petersen et al., for P17-22 WT mice (Avermann et al., 2012; Lefort et al.,  
394 2009; Tomm et al., 2014). The disadvantages of the simple 2D model is that its logistic input-  
395 output structure implies a very strong and specific assumption about the functional purpose of  
396 the circuit – to generate single spikes across a subset of neurons. Although this may be a  
397 physiologically relevant computation for this particular brain circuit (Clancy et al., 2015; Kerr et

398 al., 2007; Sato et al., 2007), it is not immediately obvious how to extend this approach to  
399 include temporal correlations, for example, or to apply it to other brain circuits where we may  
400 have less insight into their natural computations. Nevertheless, our approach demonstrates a  
401 new way to tackle such problems.

402 After building the detailed computational model of L2/3 of mouse somatosensory cortex  
403 (Figure 2), and asked how sensitive the spiking responses of the overall circuit were to  
404 changes in its underlying neural components, many of which are known to be altered in *Fmr1*  
405 KO mice (Bureau et al., 2008; Gibson et al., 2008; Gonçalves et al., 2013; Harlow et al., 2010;  
406 Hays et al., 2011; Paluszkiwicz et al., 2011; Patel et al., 2013; Testa-Silva et al., 2012). We  
407 found that while changing some neural parameters did have a large effect, changing other  
408 parameters had little or no effect on circuit function (Figure 3B). This redundancy property has  
409 been reported as widely prevalent in computational models of biological systems (Gutenkunst  
410 et al., 2007; O'Leary et al., 2015). Its existence has two important implications for studies of  
411 brain disorders: first, many of the physiological component changes discovered in animal  
412 models may be entirely benign at the circuit level. Second, any treatment designed to correct  
413 circuit function is free to push the system by arbitrary amounts along insensitive directions in  
414 parameter space without consequence, as long as it makes the correct perturbations along the  
415 sensitive directions. The insensitive directions form a null space, which is a subspace of the  
416 parameter space.

417 An important caveat to our parameter sensitivity analysis is that it was linear and local to a  
418 particular point in the high-dimensional model parameter space, corresponding to WT P17-22  
419 mice. Since the circuit dynamics are nonlinear, it is likely that the particular parameter  
420 sensitivities would be different in other parts of parameter space, especially near bifurcations  
421 where qualitatively different dynamics emerge (Hirsch et al., 2013). However, as long as the  
422 redundancy property is widely preserved, as suggested by studies on computational models of  
423 other biological systems (Fisher et al., 2013; Gutenkunst et al., 2007; Machta et al., 2013;  
424 Panas et al., 2015), then our conclusions for brain disorders remain valid.



425 In addition to the varying magnitudes of circuit components' effect on circuit function, we also  
426 found that different components shifted the circuit input-output function in different directions,  
427 as defined by our 2D logistic response model (Figures 1 and 2). Even circuit parameters that  
428 are nominally of the same type, such as the strength of glutamatergic synapses between  
429 excitatory (E) neurons in L4 to E neurons in L2/3 or synaptic strength between E neurons  
430 within L2/3, had qualitatively different effects on the circuit response to stimulation (Figure 3).  
431 According to the standard E/I imbalance model (Rubenstein and Merzenich, 2003), both of  
432 these parameters should have similar effects on circuit function; but according to the logistic  
433 response model we studied, their differing effects on slope and threshold parameters must  
434 necessarily lead to different magnitudes of change in neural firing rates and correlations  
435 (Figure 4C). Indeed, no 1-dimensional model of circuit function could ever capture the  
436 heterogeneity in parameter sensitivities that we observed (Figure 3B).

437 Next, we fit the parameters of the logistic response model to match the *in vivo* firing statistics  
438 of neural populations from WT and *Fmr1* KO mice of varying age (Figure 5). Previous studies  
439 had found that neural correlations decrease during development (Golshani et al., 2009;  
440 Rochefort et al., 2009), and that early postnatal *Fmr1* KO mice had higher correlations and  
441 firing rates than WT mice (Gonçalves et al., 2013; La Fata et al., 2014). Circuit hypersynchrony  
442 may be a general defect in autism disorders, as it is also found in mouse models of Rett  
443 syndrome (Lu et al., 2016). However, the relationship between these changes in firing statistics  
444 and the underlying neural circuit components were unclear. Our logistic model helps bridge  
445 this gap, leading to two findings: first, the direction of circuit parameter change from WT to KO  
446 was opposite in young (P9—11 and P14—16) versus mature (P30—40) animals (Figure 5C).  
447 Similar opposing switches in sensory cortex properties with age were also recently reported in  
448 *Fmr1* KO and WT rats (Berzhanskaya et al., 2016). Second, we found that the sensitivity of  
449 neural firing rates and correlations to changes in underlying circuit components depends on  
450 developmental age (Figure 6). Taken together, these findings imply that qualitatively different  
451 interventions may be needed at different stages of development in Fragile-X, and perhaps  
452 other neurodevelopmental disorders, to shift cortical circuit function towards typical wild-type  
453 operation.



454 Spontaneous, intrinsic activity is ubiquitously present in mammalian cerebral cortex. It is highly  
455 structured at multiple spatiotemporal scales (Mitra et al., 2015; Ringach, 2009) and interacts  
456 strongly with the signals evoked by sensory stimulation (Ringach, 2009). Cellular-resolution  
457 recordings in animals have shown that the patterns of spontaneous activity in neural  
458 populations are representative of the ensemble of activity patterns used by the brain to  
459 represent sensory stimuli (Berkes et al., 2011; Luczak et al., 2009; Miller et al., 2014). Here we  
460 found that the entropy of spontaneous activity in WT mouse somatosensory cortex follows an  
461 inverted-U shaped trajectory across development, and that this trajectory is dramatically  
462 altered in the *Fmr1* KO mouse model of Fragile-X (Figure 7). Although we saw no reliable  
463 differences across genotypes in early postnatal animals (P9–11), *Fmr1* KO animals showed  
464 lower entropy than WT after the second postnatal week (P14–16), while surprisingly switching  
465 to show higher entropy than WT in adult (P30–40). Notably, this switch in the direction of  
466 entropy change from WT to KO during development mirrors the reversing we saw in logistic  
467 model parameter changes in Figure 5C. Together, these findings suggest a perturbed  
468 trajectory of cortical development during the critical period in *Fmr1* KO mice (Meredith et al.,  
469 2012). However, our results cannot distinguish whether the observed perturbation in L2/3  
470 activity statistics reflects a developmental delay, or a permanently altered developmental  
471 trajectory. Further studies at later developmental time points are needed.

472 What is the functional significance of these shifts in population entropy? Previous work  
473 suggested that the entropy of neural circuit activity may be optimally tuned at intermediate  
474 levels as a trade-off between maximizing representational capacity at high entropy, versus  
475 maintaining error correction and regularization at low entropy (Schneidman et al., 2006). These  
476 properties can also be thought of as trading off between discrimination and generalization,  
477 respectively (Qian and Lipkin, 2011). If we assume that WT mice are optimally tuned, our  
478 findings predict that young *Fmr1* KO mice should show poorer somatosensory discrimination in  
479 behavioral tasks than wild-type animals, while in contrast adult *Fmr1* KO mice should perform  
480 more poorly on tasks involving generalization across somatosensory stimuli.

481 If the unidimensional E/I imbalance model is not sufficiently rich to capture the circuit changes  
482 observed in neurodevelopmental disorders, what should replace it? How many dimensions or

483 degrees of freedom should a working model for a brain disorder have? Theoretical  
484 neuroscientists have long studied E/I balance in generic models of recurrent neural circuits  
485 (Brunel, 2000; Tsodyks and Sejnowski, 1995). These models have uncovered important  
486 distinctions between ‘loose’ balanced regimes, where E and I inputs to a neuron are equal only  
487 on average, and fine-tuned ‘tight’ balanced regimes where E and I inputs to a neuron track  
488 each other closely on fast timescales (Deneve and Machens, 2016; Hennequin et al., 2017). In  
489 principle these generic models could be used to investigate multidimensional E/I imbalances in  
490 brain disorders (Vogels and Abbott, 2007). However, it is currently difficult to directly fit these  
491 many-parameter network models to data (although see Arakaki et al., 2017; Fisher et al., 2013;  
492 Stringer et al., 2016), and they are agnostic to circuit function. Instead we suggest an  
493 alternative, complementary approach: start by assuming a computational function for the  
494 particular neural circuit under study, then work backwards to design a model that is both  
495 sophisticated enough to capture the key information processing features of the circuit, but  
496 simple enough to interpret and link to physiological data. In this study we considered a 2-  
497 parameter model of L2/3 somatosensory cortex’s input-output function, which could account  
498 for both neural firing rates and correlations. Other brain circuits may demand models with more  
499 degrees of freedom. Crucially, the most informative models need not be those that include the  
500 highest level of physiological detail. All models are ultimately wrong in the sense that they  
501 make abstractions about their underlying parts, and detailed models carry the additional  
502 burden of fitting many parameters, which may be difficult to adequately constrain (O’Leary et  
503 al., 2015). Nonetheless, some models are useful (Box, 1979).

504 One potential use of simple parametric circuit models such as the ones we employed here may  
505 be as a tool for rationally designing candidate intervention compounds and then screening their  
506 effects on neural population activity. For example, the current study could have been extended  
507 to fit the logistic model to neural activity data from another cohort of *Fmr1* KO mice that had  
508 received a candidate treatment, then ask if the fitted model parameters were closer in value to  
509 those from WT animals or *Fmr1* KO controls. Approaches like this could complement the  
510 traditional strategy of designing drugs based on reversing molecular deficits and then  
511 assessing the drug’s impact on animal model behavior. Indeed, our results suggest that given

512 the multi-dimensionality of circuit properties, it may prove difficult or impossible to find a single  
513 compound that can correctly reverse deficits at any age. This scenario might require a  
514 combination of drugs chosen to push circuit-level properties towards the 'correct' region of  
515 parameter space. The framework we have introduced in this study can facilitate this type of  
516 high-dimensional intervention analysis for diverse neurodevelopmental disorders.

## 517 **Materials and Methods**

<b>Key Resources Table</b>			
<b>Reagent type (species) or resource</b>	<b>Designation</b>	<b>Source or reference</b>	<b>Identifiers</b>
strain, strain background (mus musculus)	c57bl/6J strain of wild type mice	Jackson Labs	IMSR_JAX:000664
genetic reagent (mus musculus)	Fmr1 knockout mouse on a c57 background	William Greenough (originally from Dutch-Belgian Fragile X Consortium)	RRID:MGI:2665400
chemical compound, drug	OGB1 AM (Oregon Green BAPTA-1 AM)	Molecular Probes (ThermoFisher Scientific)	
Software, algorithm	ImageJ	NIH	RRID:SCR_003070
software, algorithm	BRIAN Simulator	<a href="http://briansimulator.org">http://briansimulator.org</a>	RRID:SCR_002998
software, algorithm	MATLAB	<a href="http://www.mathworks.com/products/matlab">http://www.mathworks.com/products/matlab</a>	RRID:SCR_001622

### 518 ***Mouse in vivo calcium imaging recording***

519 All Ca<sup>2+</sup> imaging data were published previously (Gonçalves et al., 2013). Briefly, data were  
520 collected from male and female C57Bl/6 wild-type and *Fmr1* KO mice at P9–40. For each  
521 group the animal numbers were: P9-11, n=13 WT and n=9 *Fmr1* KO; P14-16, n=8 WT and  
522 n=10 *Fmr1* KO; P30-40, n=7 WT and n=6 *Fmr1* KO. There were variations in the number of  
523 cells recorded from each animal. The range of cell numbers for each group were: P9-11, 49-  
524 198 cells in WT and 84-144 cells in *Fmr1* KO; P14-16, 65-119 cells in WT and 40-149 cells in  
525 *Fmr1* KO; P30-40, 60-114 cells in WT and 69-105 cells in *Fmr1* KO. Mice were anesthetized  
526 with isoflurane, and a cranial window was fitted over primary somatosensory cortex by  
527 stereotaxic coordinates. Mice were then transferred to a two-photon microscope and headfixed  
528 to the stage while still under isoflurane anesthesia. 2–4 injections of the Ca<sup>2+</sup> sensitive  
529 Oregon-Green BAPTA-1 (OGB) dye and sulforhodamine-101 (to visualize astrocytes) were  
530 injected 200 um below the dura. Calcium imaging was performed using a Ti-Sapphire  
531 Chameleon Ultra II laser (Coherent) tuned to 800 nm. Imaging in unanesthetized mice began  
532 within 30-60 min of stopping the flow of isoflurane after the last OGB injection. Images were  
533 acquired using ScanImage software (Polgruto et al., 2004) written in MATLAB (MathWorks;

534 RRID:SCR\_001622). Whole-field images were collected using a 20× 0.95 NA objective  
535 (Olympus) at an acquisition speed of 3.9 Hz (512 × 128 pixels). Several 3-minute movies were  
536 concatenated and brief segments of motion artifacts were removed (always <10 s total). Data  
537 were corrected for x–y drift. Cell contours were automatically detected and the average  $\Delta F/F$   
538 signal of each cell body was calculated at each time point. Each  $\Delta F/F$  trace was low-pass  
539 filtered using a Butterworth filter (coefficient of 0.16) and deconvolved with a 2 s single-  
540 exponential kernel (Yaksi and Friedrich, 2006). To remove baseline noise, the standard  
541 deviation of all points below zero in each deconvolved trace was calculated, multiplied by two,  
542 and set as the positive threshold level below which all points in the deconvolved trace were set  
543 to zero. Estimated firing rates of the neurons,  $r_i(t)$ , were then obtained by multiplying the  
544 deconvolved trace by a factor previously derived empirically from cell-attached recordings in  
545 vivo (Golshani et al., 2009).

#### 546 **Computational methods**

547 Data analysis and logistic model calculations were done using MATLAB (Mathworks;  
548 RRID:SCR\_001622). All simulation code is available online at  
549 [https://github.com/cianodonnell/ODonnelletal\\_2017\\_imbalances](https://github.com/cianodonnell/ODonnelletal_2017_imbalances), and the population tracking  
550 model code (O'Donnell et al., 2017) is available at  
551 <https://github.com/cianodonnell/PopulationTracking>.

#### 552 **Detailed layer 2/3 model simulations**

553 Layer 2/3 model simulations (Figures 1 and 2) were implemented with the Python-based  
554 simulator Brian 2 (<http://briansimulator.org>; RRID:SCR\_002998) (Goodman and Brette, 2009),  
555 and results analyzed with MATLAB (Mathworks; RRID:SCR\_001622). The model consisted of  
556 four populations of reciprocally connected leaky integrate-and-fire neurons representing a L2/3  
557 somatosensory barrel circuit: 1700 excitatory neurons, 70 PV inhibitory neurons, 115 5HT<sub>3A</sub>R  
558 inhibitory neurons, and 45 SOM inhibitory neurons, driven by a separate population of 1500  
559 excitatory spike sources representing input from L4. Cell numbers were estimated by  
560 combining layer-specific excitatory and inhibitory cell count information from (Lefort et al.,  
561 2009) with the approximate percentages of the three inhibitory cell groups given by (Petersen  
562 and Crochet, 2013). The voltage  $V$  of each neuron evolved as

563 
$$\frac{dV}{dt} = (R_{in}(g_e(E_{rev,e} - V) + g_i(E_{rev,i} - V)) - (V - V_{rest}))/\tau_m$$

564 where  $R_{in}$  is the input resistance,  $E_{rev,e}$  and  $E_{rev,i}$  are the excitatory and inhibitory synaptic  
565 reversal potentials respectively,  $\tau_m$  is the membrane time constant, and  $g_e$  and  $g_i$  are the  
566 summed excitatory and inhibitory synaptic input conductances respectively. Between input  
567 events the total excitatory synaptic conductance  $g_e$  evolved in time according to the equation

574 
$$\frac{dg_e}{dt} = -g_e/\tau_{syn,e}$$

568 where  $\tau_{syn,e}$  is the excitatory synaptic time constant. Similar equations governed the inhibitory  
569 conductances. When a spike arrived at a synapse, a Bernoulli random number was drawn with  
570 release probability set according to the particular synaptic connection type. If this number was  
571 equal to one, then the total synaptic conductance for that neuron was instantaneously  
572 incremented by the specific amplitude of the chosen conductance for that individual synapse,  
573 indexed  $j$ :  $g_e \rightarrow g_e + \bar{g}_j$ .

575 All synaptic connections were formed probabilistically by drawing independent random  
576 Bernoulli variables with connection type-specific probabilities. Synaptic PSP amplitudes were  
577 drawn independently for each synapse from a log-normal distribution constrained by the  
578 experimentally reported mean and median values for each particular connection type. The  
579 maximum post-synaptic potential amplitude was set to 8 mV. Synapses in the model were  
580 conductance-based, but since synaptic strengths reported in the literature were typically in  
581 terms of EPSP/IPSP amplitude, in accordance with how the experiments were performed  
582 (Avermann et al., 2012), we set each maximal synaptic conductance as the value needed to  
583 generate a PSP of the desired amplitude when the target neuron started at resting potential in  
584 the case of EPSPs or -55mV in the case of IPSPs, which we computed analytically. Refractory  
585 periods were calculated as the inter-spike-interval corresponding to the maximal  
586 experimentally reported firing rate. Release probability and synaptic strength values for  
587 unconnected neurons are excluded from Table 1. Excitatory synaptic time constants were set  
588 at 2 ms, which is typical for the fast component of AMPA receptor responses, but could not be  
589 estimated from the PSP statistics in (Avermann et al., 2012) because of masking by the slower

590 membrane time constant. The mathematical form of our model meant that inhibitory synaptic  
591 time constants needed to be equal for all incoming inhibitory synapses to a neuron. We set  
592 these to 40 ms for E, 5HT<sub>3A</sub>R and SOM neurons and 16 ms for PV neurons, which were the  
593 typical values of the IPSP decay time constants in the (Avermann et al., 2012) dataset. Due to  
594 lack of direct data for this circuit, connection probabilities for synapses from L4 E neurons to E,  
595 PV and SOM L2/3 neurons was set to a reasonable cortical value of 0.15, while 5HT<sub>3A</sub>R  
596 neurons did not receive any input from L4 (Gentet et al., 2012). Similarly due to a lack of direct  
597 data, we set synaptic release probabilities for connections from L4 to L2/3 neurons to a typical  
598 cortical value of 0.25, while mean and median L4 excitatory PSP amplitudes onto L2/3 PV and  
599 SOM were set to 0.8 and 0.48 mV, respectively, to match reported data for L4 EPSP  
600 amplitudes onto L2/3 E neurons (Lefort et al., 2009). The differential equations were solved  
601 using the forward Euler method with an integration timestep of 0.01 ms. Each simulation run  
602 was 50 ms long, during which we recorded whether or not each neuron responded. In the rare  
603 cases where a neuron spiked more than once, we disregarded the extra spikes. L4 neuron  
604 dynamics were not explicitly simulated, but instead modeled only as a set of output spike trains.  
605 After selecting the subset of active L4 neurons, spike times were drawn randomly from a  
606 Gaussian distribution with standard deviation of 2 ms. We repeated the simulations 10 times  
607 for this identical input pattern to average over the noise due to probabilistic vesicle release. We  
608 repeated this procedure further 10 times for different random allocations of the 'ON' inputs.  
609 Then, a neuron's ON probability was defined as the fraction of these 10×10 = 100 simulations  
610 for which it responded with one or more spikes. Finally, we repeated the entire procedure for  
611 varying levels of L4 input sparsity.

612 For the simulations presented in Figure 3 we varied only 76 model parameters, which is 24  
613 less than the total number of 100 model parameters listed in Table 1. We excluded the four  
614 neuronal refractory periods (because in almost all simulations each neuron spiked a maximum  
615 of once, making the refractory period irrelevant), and the six connection probabilities that were  
616 fixed at zero. Finally, we grouped together the mean and median PSP amplitudes for each of  
617 the fourteen non-zero synaptic connections, so that both parameters were increased or



618 decreased by the same fraction in tandem. Together these choices reduced the number of test  
 619 parameters from 100 to 76.

620 For all parameters that naturally range from 0 upwards, such as the number of neurons or  
 621 release probability, we increased or decreased their values during testing in the most intuitive  
 622 way, by adding +/- 20% of the baseline value. However, this method was less useful for other  
 623 parameters, such as cell resting voltage, for which we reasoned it made more sense to scale  
 624 relative to another parameter, such as spike threshold. As a result, we varied 1) resting voltage  
 625 relative to its difference from spike threshold; 2) spike threshold relative to its difference with  
 626 resting voltage; 3) excitatory synaptic reversal potentials relative to resting voltage; 4) inhibitory  
 627 synaptic reversal potentials relative to spike threshold.

Parameter	Value	Source	+20% effect on slope, thresh	Parameter	Value	Source	+20% effect on slope, thresh
$N_E$	1700	[1]	slope: $6.4 \times 10^{-3}$ thresh: 5.16	$pcon_{I5htE}$	0.465	[2]	slope: $-3.25 \times 10^{-3}$ thresh: -0.103
$N_{I_{pv}}$	70	[1]	slope: $4.3 \times 10^{-3}$ thresh: -1.51	$pcon_{I5htI_{pv}}$	0.38	[2]	slope: $-7.13 \times 10^{-3}$ thresh: -0.298
$N_{I5ht}$	115	[1]	slope: -0.0104 thresh: -0.58	$pcon_{I5htI5ht}$	0.38	[2]	slope: $6.07 \times 10^{-4}$ thresh: 0.175
$N_{I_{som}}$	45	[1]	slope: -0.001 thresh: -0.83	$pcon_{I5htI_{som}}$	0	No data	Not tested
$N_{EL4}$	1500	[1]	slope: -0.106 thresh: 3.43	$pcon_{I_{som}E}$	0.5	[5]	slope: $-6.29 \times 10^{-3}$ thresh: -0.8919
$V_{restE}$	-68 mV	[2]	slope: 0.049 thresh: -6.09	$pcon_{I_{som}I_{pv}}$	0	No data	Not tested
$V_{restI_{pv}}$	-68 mV	[2]	slope: -0.016 thresh: -0.963	$pcon_{I_{som}I5ht}$	0	No data	Not tested
$V_{restI5ht}$	-62 mV	[2]	slope: $-9.48 \times 10^{-4}$ thresh: 0.205	$pcon_{I_{som}I_{som}}$	0	No data	Not tested
$V_{restI_{som}}$	-57 mV	[3]	slope: $3.58 \times 10^{-3}$ thresh: 0.034	$pre_{EL4E}$	0.25	No data	slope: -0.112 thresh: 4.21
$V_{thE}$	-38 mV	[2]	slope: $-3.76 \times 10^{-3}$ thresh: -0.381	$pre_{EL4I_{pv}}$	0.25	No data	slope: 0.0103 thresh: 0.682
$V_{thI_{pv}}$	-37.4 mV	[2]	slope: $3.87 \times 10^{-3}$ thresh: 0.221	$pre_{EL4I_{som}}$	0.25	No data	slope: $-2.06 \times 10^{-3}$ thresh: -0.537
$V_{thI5ht}$	-36 mV	[2]	slope: $-1.12 \times 10^{-3}$ thresh: 0.013	$pre_{EE}$	0.25	No data	slope: $4.99 \times 10^{-3}$ thresh: 6.074
$V_{thI_{som}}$	-40 mV	[3]	slope: $-3.26 \times 10^{-3}$ thresh: -0.083	$pre_{E_{I_{pv}}}$	0.25	No data	slope: $-4.04 \times 10^{-4}$ thresh: 0.163
$R_{inE}$	160 MΩ	[2]	slope: $1.95 \times 10^{-3}$ thresh: -0.283	$pre_{E_{I5ht}}$	0.25	No data	slope: $-9.32 \times 10^{-3}$ thresh: -0.532
$R_{inI_{pv}}$	100 MΩ	[2]	slope: $-8.38 \times 10^{-3}$ thresh: -0.283	$pre_{E_{I_{som}}}$	0.25	No data	slope: $-7.32 \times 10^{-3}$ thresh: -0.3847
$R_{inI5ht}$	200 MΩ	[2]	slope: $-3.87 \times 10^{-3}$ thresh: -0.653	$pre_{I_{pv}E}$	0.25	No data	slope: $1.03 \times 10^{-2}$ thresh: -0.941
$R_{inI_{som}}$	250 MΩ	[4]	slope: $7.55 \times 10^{-3}$ thresh: 0.465	$pre_{I_{pv}I_{pv}}$	0.25	No data	slope: $1.21 \times 10^{-3}$ thresh: -0.061



$\tau m_E$	28 ms	[2]	slope: $-9.59 \times 10^{-3}$ thresh: 0.268	$prel_{I_{pv}I_{5ht}}$	0.25	No data	slope: $-4.73 \times 10^{-3}$ thresh: 0.011
$\tau m_{I_{pv}}$	21 ms	[2]	slope: $4.82 \times 10^{-3}$ thresh: 0.027	$prel_{I_{5ht}E}$	0.25	No data	slope: $-1.63 \times 10^{-3}$ thresh: -0.379
$\tau m_{I_{5ht}}$	10 ms	[2]	slope: $-5.09 \times 10^{-3}$ thresh: -0.302	$prel_{I_{5ht}I_{pv}}$	0.25	No data	slope: $-3.41 \times 10^{-3}$ thresh: -0.262
$\tau m_{I_{som}}$	30 ms	[4]	slope: $-2.89 \times 10^{-3}$ thresh: -0.159	$prel_{I_{5ht}I_{5ht}}$	0.25	No data	slope: $3.05 \times 10^{-3}$ thresh: 0.123
$tref_E$	55.5 ms	[2]	Not tested	$\rho_{rel, I_{som}E}$	0.25	No data	slope: $-2.13 \times 10^{-4}$ thresh: -0.65
$tref_{I_{pv}}$	5.4 ms	[2]	Not tested	$W_{EL4E, mean}$	0.8 mV	[1]	slope: -0.142 thresh: 0.342
$tref_{I_{5ht}}$	21.3 ms	[2]	Not tested	$W_{EL4E, median}$	0.48 mV	[1]	slope: -0.142 thresh: 0.342
$tref_{I_{som}}$	20 ms	[3]	Not tested	$W_{EL4I_{pv}, mean}$	0.8 mV	$=W_{EL4E}$	slope: $3.61 \times 10^{-3}$ thresh: $6.54 \times 10^{-3}$
$\tau syn_{E,e}$	2 ms	Typical	slope: $1.37 \times 10^{-2}$ thresh: -1.79	$W_{EL4I_{pv}, median}$	0.48 mV	$=W_{EL4E}$	slope: $3.61 \times 10^{-3}$ thresh: $6.54 \times 10^{-3}$
$\tau syn_{E,i}$	40 ms	[2]	slope: $-7.29 \times 10^{-3}$ thresh: 0.48	$W_{EL4I_{som}, mean}$	0.8 mV	$=W_{EL4E}$	slope: $5.05 \times 10^{-3}$ thresh: -0.329
$\tau syn_{I_{pv},e}$	2 ms	Typical	slope: $-9.79 \times 10^{-3}$ thresh: -0.477	$W_{EL4I_{som}, median}$	0.48 mV	$=W_{EL4E}$	slope: $5.05 \times 10^{-3}$ thresh: -0.329
$\tau syn_{I_{pv},i}$	16 ms	[2]	slope: $1.56 \times 10^{-3}$ thresh: -0.097	$W_{EE, mean}$	0.37 mV	[2]	slope: $7.44 \times 10^{-3}$ thresh: 5.34
$\tau syn_{I_{5ht},e}$	2 ms	Typical	slope: $4.52 \times 10^{-3}$ thresh: -0.047	$W_{EE, median}$	0.2 mV	[2]	slope: $7.44 \times 10^{-3}$ thresh: 5.34
$\tau syn_{I_{5ht},i}$	40 ms	[2]	slope: $-3.82 \times 10^{-3}$ thresh: -0.387	$W_{EI_{pv}, mean}$	0.82 mV	[2]	slope: $-3.77 \times 10^{-4}$ thresh: -0.297
$\tau syn_{I_{som},e}$	2 ms	Typical	slope: -0.0126 thresh: $-8.82 \times 10^{-3}$	$W_{EI_{pv}, median}$	0.68 mV	[2]	slope: $-3.77 \times 10^{-4}$ thresh: -0.297
$\tau syn_{I_{som},i}$	40 ms	[2]	slope: $-4.88 \times 10^{-3}$ thresh: -0.301	$W_{EI_{5ht}, mean}$	0.39 mV	[2]	slope: $-6.81 \times 10^{-3}$ thresh: -0.46
$E_{rev_e}$	0 mV	Typical	slope: -0.056 thresh: 1.53	$W_{EI_{5ht}, median}$	0.19 mV	[2]	slope: $-6.81 \times 10^{-3}$ thresh: -0.46
$E_{rev_{Ei}}$	-68 mV	$=V_{rest_E}$	slope: $3.2 \times 10^{-3}$ thresh: -3.77	$W_{EI_{som}, mean}$	0.5 mV	No data	slope: $-3.61 \times 10^{-3}$ thresh: -0.359
$E_{rev_{I_{pvi}}}$	-68 mV	$=V_{rest_{I_{pv}}}$	slope: -0.010 thresh: -0.617	$W_{EI_{som}, median}$	0.4 mV	No data	slope: $-3.61 \times 10^{-3}$ thresh: -0.359
$E_{rev_{I_{5hti}}}$	-62 mV	$=V_{rest_{I_{5ht}}}$	slope: $3.8 \times 10^{-3}$ thresh: 0.132	$W_{I_{pv}E, mean}$	0.52 mV	[2]	slope: $6.41 \times 10^{-3}$ thresh: -1.47
$E_{rev_{I_{somi}}}$	-57 mV	$=V_{rest_{I_{som}}}$	slope: $-4.2 \times 10^{-3}$ thresh: -0.088	$W_{I_{pv}E, median}$	-0.29 mV	[2]	slope: $6.41 \times 10^{-3}$ thresh: -1.47
$\rho con_{EL4E}$	0.15	No data	slope: -0.121 thresh: 2.99	$W_{I_{pv}I_{pv}, mean}$	-0.56 mV	[2]	slope: $-2.52 \times 10^{-3}$ thresh: -0.345
$\rho con_{EL4I_{pv}}$	0.15	No data	slope: $1.38 \times 10^{-3}$ thresh: 0.029	$W_{I_{pv}I_{pv}, median}$	-0.44 mV	[2]	slope: $-2.52 \times 10^{-3}$ thresh: -0.345
$\rho con_{EL4I_{5ht}}$	0	No data	Not tested	$W_{I_{pv}I_{5ht}, mean}$	-0.83 mV	[2]	slope: $-4.24 \times 10^{-3}$ thresh: -0.266
$\rho con_{EL4I_{som}}$	0.15	No data	slope: $7.62 \times 10^{-3}$ thresh: -0.245	$W_{I_{pv}I_{5ht}, median}$	-0.6 mV	[2]	slope: $-4.24 \times 10^{-3}$ thresh: -0.266
$\rho con_{EE}$	0.17	[2]	slope: $5.86 \times 10^{-3}$ thresh: 6.084	$W_{I_{5ht}E, mean}$	-0.49 mV	[2]	slope: $-3.61 \times 10^{-4}$ thresh: -0.018
$\rho con_{EI_{pv}}$	0.575	[2]	slope: $-1.17 \times 10^{-3}$ thresh: -0.099	$W_{I_{5ht}E, median}$	-0.3 mV	[2]	slope: $-3.61 \times 10^{-4}$ thresh: -0.018
$\rho con_{EI_{5ht}}$	0.24	[2]	slope: $-6.44 \times 10^{-3}$ thresh: -0.541	$W_{I_{5ht}I_{pv}, mean}$	-0.49 mV	[2]	slope: $-1.77 \times 10^{-3}$ thresh: -0.187
$\rho con_{EI_{som}}$	0.5	[5]	slope: $-4.37 \times 10^{-3}$ thresh: -0.27	$W_{I_{5ht}I_{pv}, median}$	-0.15 mV	[2]	slope: $-1.77 \times 10^{-3}$ thresh: -0.187

$pcon_{I_{pv}E}$	0.6	[2]	slope: $7.16 \times 10^{-3}$ thresh: -1.049	$W_{I_{5ht}I_{5ht},mean}$	-0.37 mV	[2]	slope: $-4.12 \times 10^{-3}$ thresh: -0.416
$pcon_{I_{pv}I_{pv}}$	0.55	[2]	slope: $-2.61 \times 10^{-3}$ thresh: -0.0456	$W_{I_{5ht}I_{5ht},median}$	-0.23 mV	[2]	slope: $-4.12 \times 10^{-3}$ thresh: -0.416
$pcon_{I_{pv}I_{5ht}}$	0.24	[2]	slope: $-2.81 \times 10^{-3}$ thresh: -0.458	$W_{I_{5ht}E,mean}$	-0.5 mV	No data	slope: -0.013 thresh: -0.984
$pcon_{I_{pv}I_{som}}$	0	No data	Not tested	$W_{I_{5ht}E,median}$	-0.4 mV	No data	slope: -0.013 thresh: -0.984

628 Source [1] is (Lefort et al., 2009), [2] is (Avermann et al., 2012), [3] is (Fanselow et al., 2008),  
 629 [4] is (Kinnischtzke et al., 2012), [5] is (Fino and Yuste, 2011).  $N$  is number of neurons,  $V_{rest}$  is  
 630 resting potential,  $V_{th}$  is spike voltage threshold,  $R_{in}$  is input resistance,  $\tau_{ref}$  is refractory period,  
 631  $\tau_m$  is the membrane time constant,  $\tau_{syn}$  is the synaptic time constant with the first subscript  
 632 indicating the postsynaptic neuron type and the second subscript the neurotransmitter type of  
 633 the presynaptic neuron ( $e$  or  $i$ ),  $E_{rev}$  is the synaptic reversal potential,  $pcon$  is the synaptic  
 634 connection probability,  $prel$  is the synaptic release probability,  $w$  is the mean or median post-  
 635 synaptic potential amplitude as indicated. For all neuronal parameters, the subscript indicates  
 636 the neuron type:  $E$  is L2/3 excitatory neurons,  $I_{pv}$  is PV neurons,  $I_{5ht}$  is 5HT<sub>3A</sub>R neurons,  $I_{som}$   
 637 is SOM neurons, and  $EL4$  is L4 excitatory neurons. For synaptic parameters, the first and  
 638 second subscripts indicate the pre- and post-synaptic neuron types, respectively.

639 An important caveat is that although this model may be considered detailed by some  
 640 measures, it also simplifies many aspects of L2/3 circuit. For example, we assumed that all  
 641 5HT<sub>3A</sub>R cells were homogeneous, even though they likely separate into different subclasses  
 642 with type-specific connectivity (Gentet, 2012; Petersen and Crochet, 2013). Layer 2 and layer  
 643 3 may also consist of distinct cell populations (Petersen and Crochet, 2013). Not all likely  
 644 connections were included in the model (Dalezios et al., 2002; Pfeffer et al., 2013), and  
 645 connectivity was assumed to be random, even though it is likely non-random (Tomm et al.,  
 646 2014). Although these choices will likely not affect the conclusions of the current study, they  
 647 may be important to consider for future work that seeks to understand the biological function of  
 648 the L2/3 somatosensory microcircuit.

### 649 **Logistic model**

650 From the L2/3 circuit model simulations, we numerically estimated the probability  $q$  that each  
 651 neuron in the model fires a spike as a function of the fraction of L4 inputs that were active,  $f$ .  
 652 We then used the generalized linear model regression tool 'glmfit' in MATLAB to find the best

653 fit of the two logistic model parameters for each neuron:

$$654 \quad q(f) = \frac{1}{1 + \exp(-\beta(f - f_{1/2}))},$$

655 where the parameter  $\beta$  represents the slope, and the parameter  $f_{1/2}$  represents the fraction of  
656 active L4 neurons at which the response probability  $q = 0.5$ . For clarity of presentation, in the  
657 main text we converted this  $f_{1/2}$  parameter to what we termed the ‘threshold’,  $f_{thresh}$ , which we  
658 defined as the fraction of L4 neurons needed to reach a specified spike probability,  $q_{thresh}$ .  
659 Throughout the study we fixed  $q_{thresh} = 0.01$ . The threshold is related to  $f_{1/2}$  via the inverse of  
660 the logistic function

$$661 \quad f_{thresh} = f_{1/2} + \log\left(\frac{q_{thresh}}{1 - q_{thresh}}\right) / \beta.$$

662 We computed firing rates and pairwise correlations from the logistic model (Figures 3–4) in  
663 the following way. First, we assumed that the fraction of active L4 neurons is described by a  
664 normally distributed random variable with zero mean and unit variance:

$$665 \quad p(f) = \frac{\exp(-f^2/2)}{\sqrt{2\pi}} = \mathcal{N}(0,1).$$

666 We defined the  $\beta$  and  $f_{1/2}$  parameters relative to the mean and standard deviation of the input  
667 distribution. Since  $q$  is a monotonically increasing function of  $f$ , the probability distribution for  $q$   
668 is

$$676 \quad p(q) = p(f(q)) \left| \frac{df}{dq} \right|$$

669 where  $f(q)$  is the inverse of the logistic function  $q(f)$  and

$$670 \quad \frac{df}{dq} = \frac{(\exp(-\beta(f - f_{1/2})) + 1)^2}{\beta \exp(-\beta(f - f_{1/2}))}. \text{ We calculate a neuron's mean firing rate } \mu \text{ as the expectation of } q,$$

$$671 \quad \mu = \mathbb{E}[q] = \int_0^1 [q \times p(q)] dq = \int_0^1 \left[ q \times p(f(q)) \left| \frac{df}{dq} \right| \right] dq.$$

672 We calculate the pairwise covariance of two homogeneous neurons driven by a common input  
673  $f$  as

$$674 \quad \text{cov} = \mathbb{E}[q^2] - (\mathbb{E}[q])^2 = \mathbb{E}[q^2] - \mu^2 = \int_0^1 \left[ q^2 \times p(f(q)) \left| \frac{df}{dq} \right| \right] dq - \mu^2, \text{ then find the pairwise}$$

675 correlation by normalizing the covariance by the neurons' shared variance,  $\text{var} = \mu(1 - \mu)$ .

677 For fitting the logistic model to the recorded neural firing rates and correlations (Figure 5), we  
678 considered a population model where the joint probability distribution across threshold and  
679 slope was specified by a 2D Gaussian, which has five parameters: threshold mean and s.d.,  
680 slope mean and s.d., and slope-threshold correlation. The three constraint statistics we  
681 considered from the neural population data were the mean neural ON probability, the s.d. of  
682 neural ON probabilities, and the mean pairwise correlations. We found the best-fit model  
683 parameters for each dataset using stochastic gradient descent (code available at  
684 [https://github.com/cianodonnell/ODonnelletal\\_2017\\_imbalances](https://github.com/cianodonnell/ODonnelletal_2017_imbalances)). Briefly, the fitting procedure  
685 followed: 1) initialize the parameters at a starting guess points, 2) compute the predicted three  
686 output firing statistics via numerical integration over the model's probability distributions, 3)  
687 compute the fitting error as the summed squared difference between the model output  
688 predictions and the target values, 4) generate a new set of parameter values by adding a small  
689 perturbation of a zero-mean Gaussian random number to each parameter, 5) compute the new  
690 output statistics, 5) recompute the fitting error, 6) if the new error is smaller than the old error,  
691 accept the updated parameter values, otherwise reject them and revert to the old parameters,  
692 7) return to step 4 unless the error is lower than the desired tolerance. We checked for fit  
693 convergence by sampling a large number of logistic model parameters from the fitted 2D  
694 Gaussian, drawing binary samples from these logistic model neurons and computing the ON  
695 probability mean and s.d., and mean pairwise correlation from the synthetic binary samples,  
696 and comparing the computed statistical values to the original data statistics (Figure 5 –  
697 supplemental figure 1). For the sensitivity analysis presented in Figure 6, we numerically  
698 computed the partial derivative in mean firing rate and pairwise correlation with respect to the  
699 mean slope and mean threshold parameters in the population logistical model, using standard  
700 finite difference methods.

### 701 ***Statistical tests***

702 To avoid parametric assumptions, all statistical tests were done using standard bootstrapping  
703 methods with custom-written MATLAB scripts. For example when assessing the observed  
704 difference between two group means  $\Delta\mu_{\text{obs}}$  we performed the following procedure to calculate  
705 a p-value. First we pool the data points from the two groups to create a null set  $S_{\text{null}}$ . We then

706 construct two hypothetical groups of samples  $S_1$  and  $S_2$  from this by randomly drawing  $n_1$  and  
707  $n_2$  samples with replacement from  $S_{\text{null}}$ , where  $n_1$  and  $n_2$  are the number of data points in the  
708 original groups 1 and 2 respectively. We take the mean of both hypothetical sets  $\Delta\mu_1$  and  $\Delta\mu_2$   
709 and calculate their difference  $\Delta\mu_{\text{null}} = \Delta\mu_1 - \Delta\mu_2$ . We then repeat the entire procedure  $10^7$   
710 times to build up a histogram of  $\Delta\mu_{\text{null}}$ . This distribution is always centered at zero. After  
711 normalizing, this can be interpreted as the probability distribution  $f(\Delta\mu_{\text{null}})$  for observing a group  
712 mean difference of  $\Delta\mu_{\text{null}}$  purely by chance if the data were actually sampled from the same  
713 null distribution. Then the final p-value for the probability of finding a group difference of at  
714 least  $\Delta\mu_{\text{obs}}$  in either direction is given by  $p = \int_{-\infty}^{-\Delta\mu_{\text{obs}}} f(\Delta\mu_{\text{null}})d\Delta\mu_{\text{null}} + \int_{\Delta\mu_{\text{obs}}}^{\infty} f(\Delta\mu_{\text{null}})d\Delta\mu_{\text{null}}$ .  
715 For Figure 5C we estimated 2-dimensional 95% confidence ellipses for the shift in mean slope-  
716 threshold parameters between Fmr1 KO and WT by computing the sample error variances and  
717 covariance through bootstrapping. Then the 95% confidence ellipse can be computed using  
718 the Chi-squared distribution. We plotted the confidence interval ellipse using the MATLAB  
719 function `error_ellipse.m`, downloaded from  
720 <https://www.mathworks.com/matlabcentral/fileexchange/4705-error-ellipse>.

### 721 ***Conversion from firing rate to ON/OFF probabilities for $\text{Ca}^{2+}$ imaging data***

722 For the  $\text{Ca}^{2+}$  imaging data, we began with estimated firing rate time series  $r_i(t)$  for each neuron  
723  $i$  recorded as part of a population of  $N$  neurons. For later parts of the analysis we needed to  
724 convert these firing rates to binary ON/OFF values. This conversion involves a choice. One  
725 option would be to simply threshold the data, but this would throw away information about the  
726 magnitude of the firing rate. We instead take a probabilistic approach where rather than  
727 deciding definitively whether a given neuron was ON or OFF in a given time bin, we calculate  
728 the probability that the neuron was ON or OFF by assuming that neurons fire action potentials  
729 according to an inhomogeneous Poisson process with rate  $r_i(t)$ . The mean number of spikes  
730  $\lambda_i(t)$  expected in a time bin of width  $\Delta t$  is  $\lambda_i(t) = r_i(t)\Delta t$ . We choose  $\Delta t = 1$  second. Under the  
731 Poisson model the actual number of spikes  $m$  in a particular time bin is a random variable that  
732 follows the Poisson distribution  $P(m=k) = \lambda^k \exp(-\lambda) / k!$ . We considered a neuron active (ON) if  
733 it is firing one or more spikes in a given time bin. Hence the probability that a neuron is ON is  
734  $p_{\text{on}}(t) = 1 - P(m=0) = 1 - \exp(-\lambda)$ . This approach has two advantages over thresholding: 1) it

735 preserves some information about the magnitude of firing rates, and 2) it acts to regularize the  
736 probability distribution for the number of neurons active by essentially smoothing nearby  
737 values together.

### 738 ***Entropy estimation for large numbers of neurons***

739 Entropy was estimated by fitting a statistical model we recently developed, called the  
740 population tracking model (O'Donnell et al., 2017), to the binarized  $\text{Ca}^{2+}$  imaging data. Briefly,  
741 the population tracking model fits two aspects of the data: the probability distribution for the  
742 number of neurons synchronously active in the population, and also the conditional firing  
743 probability that each individual neuron is active given the population count. Hence the model  
744 captures both some aggregate statistics of the population activity, and some aspects of the  
745 heterogeneity across neurons. See (O'Donnell et al., 2017) for complete details and validation  
746 of the method. Code for fitting the model to data is available at  
747 <https://github.com/cianodonnell/PopulationTracking>.

748 The entropy/neuron generally decreased with the number of neurons considered as result of  
749 the population correlations (Figure 7B), so we needed to control for neural population size  
750 when comparing data from different experimental groups. On the one hand, we would like to  
751 study as large a number of neurons as possible, because we expect the effects of collective  
752 network dynamics to be stronger for large population sizes and this may be the regime where  
753 differences between the groups emerge. On the other hand, our recording methods allowed us  
754 to sample only typically around  $\sim 100$  neurons at a time, and as few as 40 neurons in some  
755 animals. Hence we proceeded by first estimating the entropy/neuron in each animal by  
756 calculating the entropy of random subsets of neurons of varying size from 10 to 100 (if  
757 possible) in steps of 10. For each population size we sampled a large number of independent  
758 subsets, calculated the entropy of each. Finally, for each dataset we fit a double exponential  
759 function to the estimated entropy/neuron as a function of the number of neurons:  $H/N =$   
760  $A \cdot \exp(-b \cdot N) + C \cdot \exp(-d \cdot N) + e$ , and used this fit to estimate  $H/N$  for 100 neurons.

### 761 **Acknowledgements**

762 We thank Timothy O'Leary, Hannes Saal, and Alex Williams for comments on earlier versions

763 of the manuscript. This study was supported by funding from FRAXA Research Foundation,  
764 Howard Hughes Medical Institute, Sloan-Swartz Foundation, the Dana Foundation,  
765 Developmental Disabilities Translational Research Program grant #20160969 (The John  
766 Merck Fund), SFARI grant 295438 (Simons Foundation) and the NIH (NICHD R01HD054453  
767 and NINDS RC1NS068093).

#### 768 **Competing Interests**

769 The authors have no competing interests to declare.



770 **References**

- 771 Arakaki, T., Barello, G., Ahmadian, Y., 2017. Capturing the diversity of biological tuning curves  
772 using generative adversarial networks. arXiv.
- 773 Avermann, M., Tomm, C., Mateo, C., Gerstner, W., Petersen, C.C.H., 2012. Microcircuits of  
774 excitatory and inhibitory neurons in layer 2/3 of mouse barrel cortex. *J Neurophysiol* 107,  
775 3116–3134. doi:10.1152/jn.00917.2011
- 776 Bateup, H.S., Takasaki, K.T., Saulnier, J.L., Deneffrio, C.L., Sabatini, B.L., 2011. Loss of Tsc1  
777 in vivo impairs hippocampal mGluR-LTD and increases excitatory synaptic function. *J*  
778 *Neurosci* 31, 8862–8869. doi:10.1523/JNEUROSCI.1617-11.2011
- 779 Belmonte, M.K., Allen, G., Beckel-Mitchener, A., Boulanger, L.M., Carper, R.A., Webb, S.J.,  
780 2004. Autism and abnormal development of brain connectivity. *J Neurosci* 24, 9228–9231.  
781 doi:10.1523/JNEUROSCI.3340-04.2004
- 782 Berkes, P., Orbán, G., Lengyel, M., Fiser, J., 2011. Spontaneous cortical activity reveals  
783 hallmarks of an optimal internal model of the environment. *Science* 331, 83–87.  
784 doi:10.1126/science.1195870
- 785 Berzhanskaya, J., Phillips, M.A., Shen, J., Colonnese, M.T., 2016. Sensory hypo-excitability in  
786 a rat model of fetal development in Fragile X Syndrome. *Sci Rep* 6, 30769.  
787 doi:10.1038/srep30769
- 788 Box, G. E. P., 1979. Robustness in the strategy of scientific model building, in Launer, R. L.;  
789 Wilkinson, G. N., *Robustness in Statistics, Academic Press*, pp. 201–236.)
- 790 Braat, S., Kooy, R.F., 2015. The GABAA Receptor as a Therapeutic Target for  
791 Neurodevelopmental Disorders. *Neuron* 86, 1119–1130. doi:10.1016/j.neuron.2015.03.042
- 792 Brunel, N., 2000. Dynamics of sparsely connected networks of excitatory and inhibitory spiking  
793 neurons. *J Comput Neurosci* 8, 183–208.
- 794 Bureau, I., Shepherd, G.M.G., Svoboda, K., 2008. Circuit and plasticity defects in the  
795 developing somatosensory cortex of FMR1 knock-out mice. *J Neurosci* 28, 5178–5188.  
796 doi:10.1523/JNEUROSCI.1076-08.2008
- 797 Clancy, K.B., Schnepel, P., Rao, A.T., Feldman, D.E., 2015. Structure of a single whisker  
798 representation in layer 2 of mouse somatosensory cortex. *J Neurosci* 35, 3946–3958.

- 799       doi:10.1523/JNEUROSCI.3887-14.2015
- 800 Contractor, A., Klyachko, V.A., Portera-Cailliau, C., 2015. Altered Neuronal and Circuit  
801       Excitability in Fragile X Syndrome. *Neuron* 87, 699–715. doi:10.1016/j.neuron.2015.06.017
- 802 Cover, T.M., Thomas, J.A., 2006. *Elements of Information Theory*, 2nd ed. Wiley-Interscience.
- 803 Cruz-Martin, A., Crespo, M., Portera-Cailliau, C., 2010. Delayed Stabilization of Dendritic  
804       Spines in Fragile X Mice. *J Neurosci* 30, 7793–7803. doi:10.1523/JNEUROSCI.0577-  
805       10.2010
- 806 Dalezios, Y., Luján, R., Shigemoto, R., Roberts, J.D.B., Somogyi, P., 2002. Enrichment of  
807       mGluR7a in the presynaptic active zones of GABAergic and non-GABAergic terminals on  
808       interneurons in the rat somatosensory cortex. *Cereb Cortex* 12, 961–974.
- 809 Dani, V.S., Chang, Q., Maffei, A., Turrigiano, G.G., Jaenisch, R., Nelson, S.B., 2005. Reduced  
810       cortical activity due to a shift in the balance between excitation and inhibition in a mouse  
811       model of Rett syndrome. *Proc. Natl. Acad. Sci. U.S.A.* 102, 12560–12565.  
812       doi:10.1073/pnas.0506071102
- 813 Deneve, S., Machens, C.K., 2016. Efficient codes and balanced networks. *Nature Publishing*  
814       Group 19, 375–382. doi:10.1038/nn.4243
- 815 Elstrott, J., Clancy, K.B., Jafri, H., Akimenko, I., Feldman, D.E., 2014. Cellular mechanisms for  
816       response heterogeneity among L2/3 pyramidal cells in whisker somatosensory cortex. *J*  
817       *Neurophysiol* 112, 233–248. doi:10.1152/jn.00848.2013
- 818 Fanselow, E.E., Richardson, K.A., Connors, B.W., 2008. Selective, state-dependent activation  
819       of somatostatin-expressing inhibitory interneurons in mouse neocortex. *J Neurophysiol* 100,  
820       2640–2652. doi:10.1152/jn.90691.2008
- 821 Fino, E., Yuste, R., 2011. Dense inhibitory connectivity in neocortex. *Neuron* 69, 1188–1203.  
822       doi:10.1016/j.neuron.2011.02.025
- 823 Fisher, D., Olasagasti, I., Tank, D.W., Aksay, E.R.F., Goldman, M.S., 2013. A modeling  
824       framework for deriving the structural and functional architecture of a short-term memory  
825       microcircuit. *Neuron* 79, 987–1000. doi:10.1016/j.neuron.2013.06.041
- 826 Frye, C.G., Maclean, J.N., 2016. Spontaneous activations follow a common developmental  
827       course across primary sensory areas in mouse neocortex. *J Neurophysiol* 116, 431–437.  
828       doi:10.1152/jn.00172.2016

- 829 Gentet, L.J., 2012. Functional diversity of supragranular GABAergic neurons in the barrel  
830 cortex. *Front Neural Circuits* 6, 52. doi:10.3389/fncir.2012.00052
- 831 Gentet, L.J., Kremer, Y., Taniguchi, H., Huang, Z.J., Staiger, J.F., Petersen, C.C.H., 2012.  
832 Unique functional properties of somatostatin-expressing GABAergic neurons in mouse  
833 barrel cortex. *Nat Neurosci* 15, 607–612. doi:10.1038/nn.3051
- 834 Gibson, J.R., Bartley, A.F., Hays, S.A., Huber, K.M., 2008. Imbalance of neocortical excitation  
835 and inhibition and altered UP states reflect network hyperexcitability in the mouse model of  
836 fragile X syndrome. *J Neurophysiol* 100, 2615–2626. doi:10.1152/jn.90752.2008
- 837 Golshani, P., Gonçalves, J.T., Khoshkhoo, S., Mostany, R., Smirnakis, S., Portera-Cailliau, C.,  
838 2009. Internally mediated developmental desynchronization of neocortical network activity.  
839 *J Neurosci* 29, 10890–10899. doi:10.1523/JNEUROSCI.2012-09.2009
- 840 Gonçalves, J.T., Anstey, J.E., Golshani, P., Portera-Cailliau, C., 2013. Circuit level defects in  
841 the developing neocortex of Fragile X mice. *Nat Neurosci* 16, 903–909.  
842 doi:10.1038/nn.3415
- 843 Goodman, D.F.M., Brette, R., 2009. The brain simulator. *Front Neurosci* 3, 192–197.  
844 doi:10.3389/neuro.01.026.2009
- 845 Gutenkunst, R.N., Waterfall, J.J., Casey, F.P., Brown, K.S., Myers, C.R., Sethna, J.P., 2007.  
846 Universally sloppy parameter sensitivities in systems biology models. *PLoS Comput Biol* 3,  
847 1871–1878. doi:10.1371/journal.pcbi.0030189
- 848 Harlow, E.G., Till, S.M., Russell, T.A., Wijetunge, L.S., Kind, P., Contractor, A., 2010. Critical  
849 period plasticity is disrupted in the barrel cortex of FMR1 knockout mice. *Neuron* 65, 385–  
850 398. doi:10.1016/j.neuron.2010.01.024
- 851 Hays, S.A., Huber, K.M., Gibson, J.R., 2011. Altered neocortical rhythmic activity states in  
852 *Fmr1* KO mice are due to enhanced mGluR5 signaling and involve changes in excitatory  
853 circuitry. *J Neurosci* 31, 14223–14234. doi:10.1523/JNEUROSCI.3157-11.2011
- 854 He, Q., Nomura, T., Xu, J., Contractor, A., 2014. The developmental switch in GABA polarity is  
855 delayed in fragile X mice. *J Neurosci* 34, 446–450. doi:10.1523/JNEUROSCI.4447-13.2014
- 856 Hennequin, G., Agnes, E.J., Vogels, T.P., 2017. Inhibitory Plasticity: Balance, Control, and  
857 Codependence. *Annu. Rev. Neurosci.* 40, annurev-neuro-072116-031005.  
858 doi:10.1146/annurev-neuro-072116-031005

- 859 Hirsch, M.W., Smale, S., Devaney, R.L., 2013. Differential Equations, Dynamical Systems, and  
860 an Introduction to Chaos, 3rd ed. Academic Press.
- 861 Kehrer, C., Maziashvili, N., Dugladze, T., Gloveli, T., 2008. Altered Excitatory-Inhibitory  
862 Balance in the NMDA-Hypofunction Model of Schizophrenia. *Frontiers in Molecular*  
863 *Neuroscience* 1, 6. doi:10.3389/neuro.02.006.2008
- 864 Kerr, J.N.D., de Kock, C.P.J., Greenberg, D.S., Bruno, R.M., Sakmann, B., Helmchen, F., 2007.  
865 Spatial organization of neuronal population responses in layer 2/3 of rat barrel cortex. *J*  
866 *Neurosci* 27, 13316–13328. doi:10.1523/JNEUROSCI.2210-07.2007
- 867 Kinnischtzke, A.K., Sewall, A.M., Berkepile, J.M., Fanselow, E.E., 2012. Postnatal maturation  
868 of somatostatin-expressing inhibitory cells in the somatosensory cortex of GIN mice. *Front*  
869 *Neural Circuits* 6, 33. doi:10.3389/fncir.2012.00033
- 870 La Fata, G., Gärtner, A., Domínguez-Iturza, N., Dresselaers, T., Dawitz, J., Poorthuis, R.B.,  
871 Avena, M., Himmelreich, U., Meredith, R.M., Achsel, T., Dotti, C.G., Bagni, C., 2014.  
872 FMRP regulates multipolar to bipolar transition affecting neuronal migration and cortical  
873 circuitry. *Nat Neurosci*. doi:10.1038/nn.3870
- 874 Lee, E., Lee, J., Kim, E., 2017. Excitation/Inhibition Imbalance in Animal Models of Autism  
875 Spectrum Disorders. *Biol. Psychiatry* 81, 838–847. doi:10.1016/j.biopsych.2016.05.011
- 876 Lefort, S., Tómm, C., Floyd Sarria, J.-C., Petersen, C.C.H., 2009. The excitatory neuronal  
877 network of the C2 barrel column in mouse primary somatosensory cortex. *Neuron* 61, 301–  
878 316. doi:10.1016/j.neuron.2008.12.020
- 879 Lu, H., Ash, R.T., He, L., Kee, S.E., Wang, W., Yu, D., Hao, S., Meng, X., Ure, K., Ito-Ishida, A.,  
880 Tang, B., Sun, Y., Ji, D., Tang, J., Arenkiel, B.R., Smirnakis, S.M., Zoghbi, H.Y., 2016.  
881 Loss and Gain of MeCP2 Cause Similar Hippocampal Circuit Dysfunction that Is Rescued  
882 by Deep Brain Stimulation in a Rett Syndrome Mouse Model. *Neuron* 91, 739–747.  
883 doi:10.1016/j.neuron.2016.07.018
- 884 Luczak, A., Bartho, P., Harris, K.D., 2009. Spontaneous events outline the realm of possible  
885 sensory responses in neocortical populations. *Neuron* 62, 413–425.  
886 doi:10.1016/j.neuron.2009.03.014
- 887 Machta, B.B., Chachra, R., Transtrum, M.K., Sethna, J.P., 2013. Parameter space  
888 compression underlies emergent theories and predictive models. *Science* 342, 604–607.

- 889       doi:10.1126/science.1238723
- 890   Mao, T., Kusefoglou, D., Hooks, B.M., Huber, D., Petreanu, L., Svoboda, K., 2011. Long-range  
891       neuronal circuits underlying the interaction between sensory and motor cortex. *Neuron* 72,  
892       111–123. doi:10.1016/j.neuron.2011.07.029
- 893   Meredith, R.M., Dawitz, J., Kramvis, I., 2012. Sensitive time-windows for susceptibility in  
894       neurodevelopmental disorders. *Trends Neurosci* 35, 335–344.  
895       doi:10.1016/j.tins.2012.03.005
- 896   Miller, J.-E.K., Ayzenshtat, I., Carrillo-Reid, L., Yuste, R., 2014. Visual stimuli recruit  
897       intrinsically generated cortical ensembles. 111, E4053–E4061.  
898       doi:10.1073/pnas.1406077111
- 899   Mitra, A., Snyder, A.Z., Blazey, T., Raichle, M.E., 2015. Lag threads organize the brain's  
900       intrinsic activity. *Proc. Natl. Acad. Sci. U.S.A.* 112, E2235–E2244.  
901       doi:10.1073/pnas.1503960112
- 902   Nelson, S.B., Valakh, V., 2015. Excitatory/Inhibitory Balance and Circuit Homeostasis in  
903       Autism Spectrum Disorders. *Neuron* 87, 684–698. doi:10.1016/j.neuron.2015.07.033
- 904   O'Donnell, C., Gonçalves, J.T., Whiteley, N., Portera-Cailliau, C., Sejnowski, T.J., 2017. The  
905       Population Tracking Model: A Simple, Scalable Statistical Model for Neural Population  
906       Data. *Neural Comput* 29, 50–93. doi:10.1162/NECO\_a\_00910
- 907   O'Donnell, C., 2017. PopulationTracking. Github.  
908       <https://github.com/cianodonnell/PopulationTracking>. 2c9eada.
- 909   O'Donnell, C., 2017. ODonnelletal\_2017\_imbalances. Github.  
910       [https://github.com/cianodonnell/ODonnelletal\\_2017\\_imbalances](https://github.com/cianodonnell/ODonnelletal_2017_imbalances). 2383a26.
- 911   O'Leary, T., Sutton, A.C., Marder, E., 2015. Computational models in the age of large datasets.  
912       *Curr Opin Neurobiol* 32C, 87–94. doi:10.1016/j.conb.2015.01.006
- 913   Paluszkiewicz, S.M., Olmos-Serrano, J.L., Corbin, J.G., Huntsman, M.M., 2011. Impaired  
914       inhibitory control of cortical synchronization in fragile X syndrome. *J Neurophysiol* 106,  
915       2264–2272. doi:10.1152/jn.00421.2011
- 916   Panas, D., Amin, H., Maccione, A., Muthmann, O., van Rossum, M., Berdondini, L., Hennig,  
917       M.H., 2015. Sloppiness in spontaneously active neuronal networks. *J Neurosci* 35, 8480–  
918       8492. doi:10.1523/JNEUROSCI.4421-14.2015

- 919 Patel, A.B., Hays, S.A., Bureau, I., Huber, K.M., Gibson, J.R., 2013. A target cell-specific role  
920 for presynaptic Fmr1 in regulating glutamate release onto neocortical fast-spiking inhibitory  
921 neurons. *J Neurosci* 33, 2593–2604. doi:10.1523/JNEUROSCI.2447-12.2013
- 922 Petersen, C.C.H., Crochet, S., 2013. Synaptic computation and sensory processing in  
923 neocortical layer 2/3. *Neuron* 78, 28–48. doi:10.1016/j.neuron.2013.03.020
- 924 Petreanu, L., Huber, D., Sobczyk, A., Svoboda, K., 2007. Channelrhodopsin-2-assisted circuit  
925 mapping of long-range callosal projections., *Nature neuroscience*. doi:10.1038/nn1891
- 926 Pfeffer, C.K., Xue, M., He, M., Huang, Z.J., Scanziani, M., 2013. Inhibition of inhibition in visual  
927 cortex: the logic of connections between molecularly distinct interneurons. *Nat Neurosci*.  
928 doi:10.1038/nn.3446
- 929 Pologruto, T.A., Yasuda, R., Svoboda, K., 2004. Monitoring neural activity and [Ca<sup>2+</sup>] with  
930 genetically encoded Ca<sup>2+</sup> indicators. *J Neurosci* 24, 9572–9579.  
931 doi:10.1523/JNEUROSCI.2854-04.2004
- 932 Qian, N., Lipkin, R.M., 2011. A learning-style theory for understanding autistic behaviors. *Front*  
933 *Hum Neurosci* 5, 77. doi:10.3389/fnhum.2011.00077
- 934 Quian Quiroga, R., Panzeri, S., 2009. Extracting information from neuronal populations:  
935 information theory and decoding approaches. *Nat Rev Neurosci* 10, 173–185.  
936 doi:10.1038/nrn2578
- 937 Ringach, D.L., 2009. Spontaneous and driven cortical activity: implications for computation.  
938 *Curr Opin Neurobiol* 19, 439–444. doi:10.1016/j.conb.2009.07.005
- 939 Rochefort, N.L., Garaschuk, O., Milos, R.-I., Narushima, M., Marandi, N., Pichler, B.,  
940 Kovalchuk, Y., Konnerth, A., 2009. Sparsification of neuronal activity in the visual cortex at  
941 eye-opening. *106*, 15049–15054. doi:10.1073/pnas.0907660106
- 942 Rubenstein, J.L.R., Merzenich, M.M., 2003. Model of autism: increased ratio of  
943 excitation/inhibition in key neural systems. *Genes Brain Behav.* 2, 255–267.
- 944 Sato, T.R., Gray, N.W., Mainen, Z.F., Svoboda, K., 2007. The functional microarchitecture of  
945 the mouse barrel cortex. *PLoS Biol* 5, e189. doi:10.1371/journal.pbio.0050189
- 946 Schneidman, E., Berry, M.J., Segev, R., Bialek, W., 2006. Weak pairwise correlations imply  
947 strongly correlated network states in a neural population. *Nature* 440, 1007–1012.  
948 doi:10.1038/nature04701



- 949 Selby, L., Zhang, C., Sun, Q.-Q., 2007. Major defects in neocortical GABAergic inhibitory  
950 circuits in mice lacking the fragile X mental retardation protein. *Neurosci. Lett.* 412, 227–  
951 232. doi:10.1016/j.neulet.2006.11.062
- 952 Stringer, C., Pachitariu, M., Steinmetz, N.A., Okun, M., Bartho, P., Harris, K.D., Sahani, M.,  
953 Lesica, N.A., 2016. Inhibitory control of correlated intrinsic variability in cortical networks.  
954 *elife* 5, 91. doi:10.7554/eLife.19695
- 955 Testa-Silva, G., Loebel, A., Giugliano, M., de Kock, C.P.J., Mansvelder, H.D., Meredith, R.M.,  
956 2012. Hyperconnectivity and slow synapses during early development of medial prefrontal  
957 cortex in a mouse model for mental retardation and autism. *Cereb Cortex* 22, 1333–1342.  
958 doi:10.1093/cercor/bhr224
- 959 The Dutch-Belgian Fragile X Consortium, 1994. Fmr1 knockout mice: a model to study fragile  
960 X mental retardation. The Dutch-Belgian Fragile X Consortium. *Cell* 78, 23–33.
- 961 Tomm, C., Avermann, M., Petersen, C., Gerstner, W., Vogels, T.P., 2014. Connection-type-  
962 specific biases make uniform random network models consistent with cortical recordings. *J*  
963 *Neurophysiol* 112, 1801–1814. doi:10.1152/jn.00629.2013
- 964 Tsodyks, M.V., Sejnowski, T., 1995. Rapid state switching in balanced cortical network models.  
965 *Network: Computation in neural systems* 111–124.
- 966 Vogels, T.P., Abbott, L.F., 2007. Gating deficits in model networks: a path to schizophrenia?  
967 *Pharmacopsychiatry* 40 Suppl 1, S73–7. doi:10.1055/s-2007-992130
- 968 Wallace, M.L., Burette, A.C., Weinberg, R.J., Philpot, B.D., 2012. Maternal loss of Ube3a  
969 produces an excitatory/inhibitory imbalance through neuron type-specific synaptic defects.  
970 *Neuron* 74, 793–800. doi:10.1016/j.neuron.2012.03.036
- 971 Wilson, H.R., Cowan, J.D., 1972. Excitatory and inhibitory interactions in localized populations  
972 of model neurons. *Biophys J* 12, 1–24. doi:10.1016/S0006-3495(72)86068-5
- 973 Yaksi, E., Friedrich, R.W., 2006. Reconstruction of firing rate changes across neuronal  
974 populations by temporally deconvolved Ca<sup>2+</sup> imaging. *Nat. Methods* 3, 377–383.  
975 doi:10.1038/nmeth874



976 **Figure Supplements**

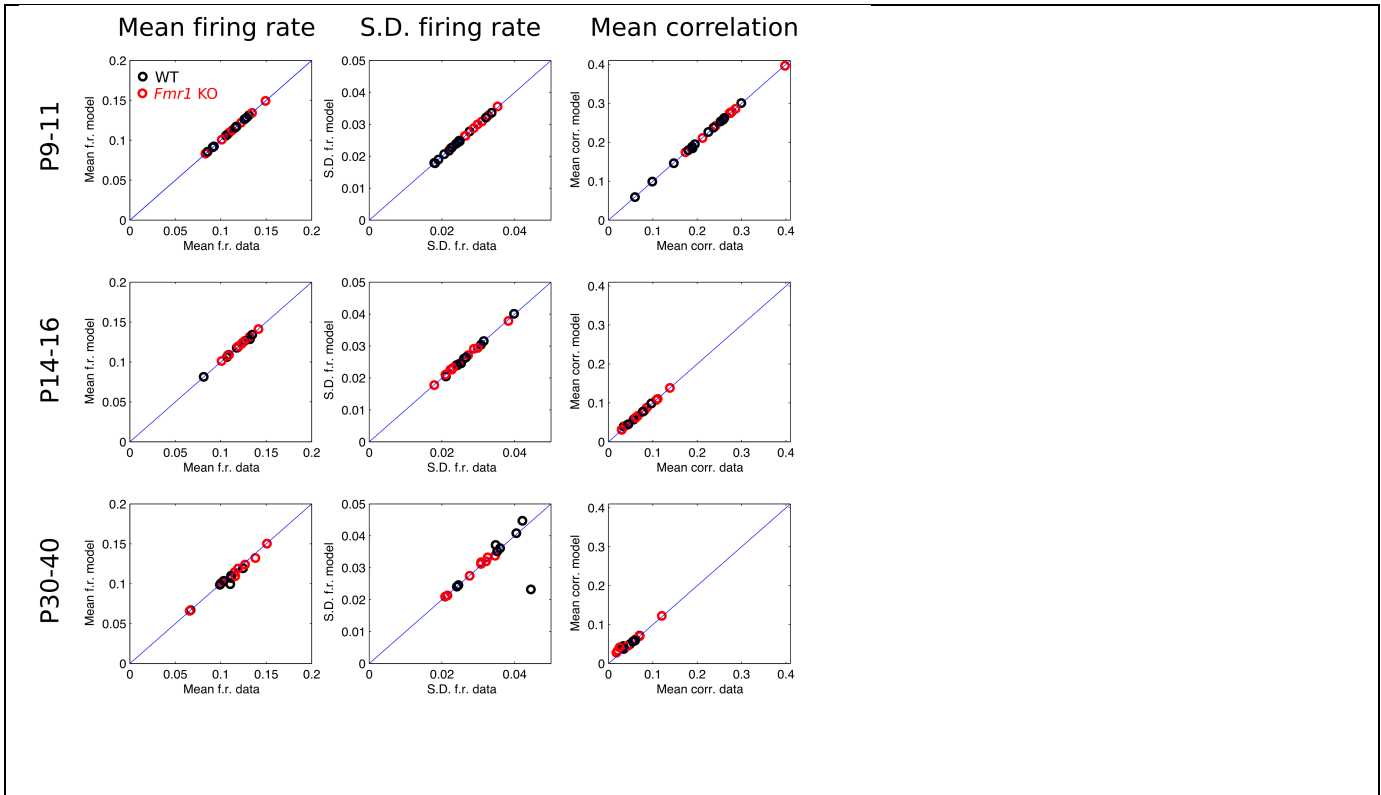


**Figure 5 – figure supplement 1. Agreement between population logistic model activity statistics and raw data statistics.**

Black circles are WT, red are *Fmr1* KO. Each data point corresponds to a recording from a single animal. Each plot shows model prediction versus raw data target value. Plots in each row correspond to data from a different age group (P9–11, P14–16, and P30–40), and each column corresponds to one of the three target activity statistics (mean firing rate, s.d. in firing rate, and mean pairwise correlation). Blue line is identity.

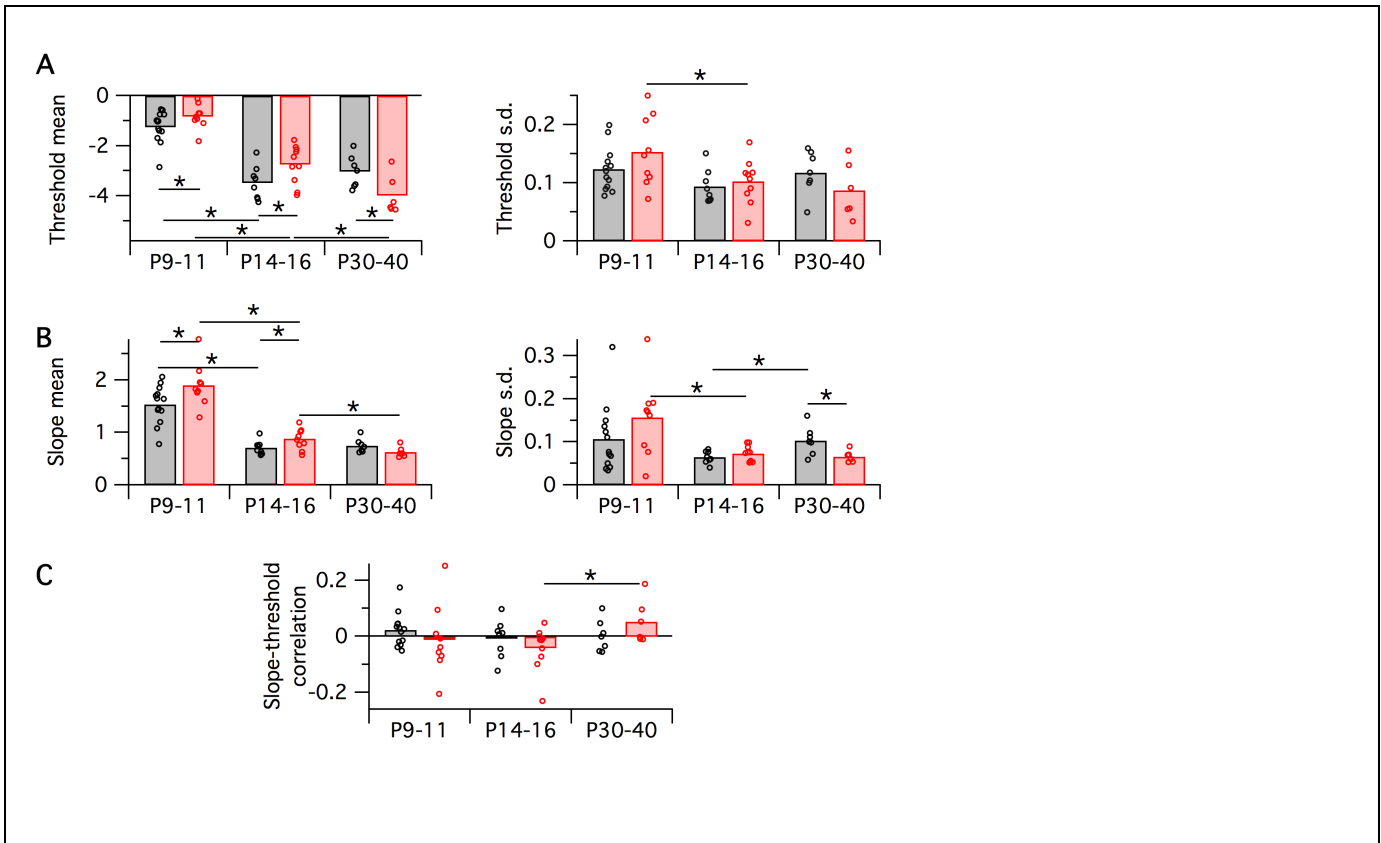


**Figure 5 – figure supplement 2. Variation in population logistic model parameter fits with developmental age group and genotype.**

Black symbols are WT, red are *Fmr1* KO. Each data point corresponds to a recording from a single animal, bars correspond to group means. In all cases, horizontal bar with asterisk indicates a significant difference in group means ( $p < 0.05$  via bootstrapping).

**A:** Logistic threshold parameter mean (left) and s.d. (right).

**B:** Logistic slope parameter mean (left) and s.d. (right).

**C:** Slope-threshold correlation parameter.

978

979

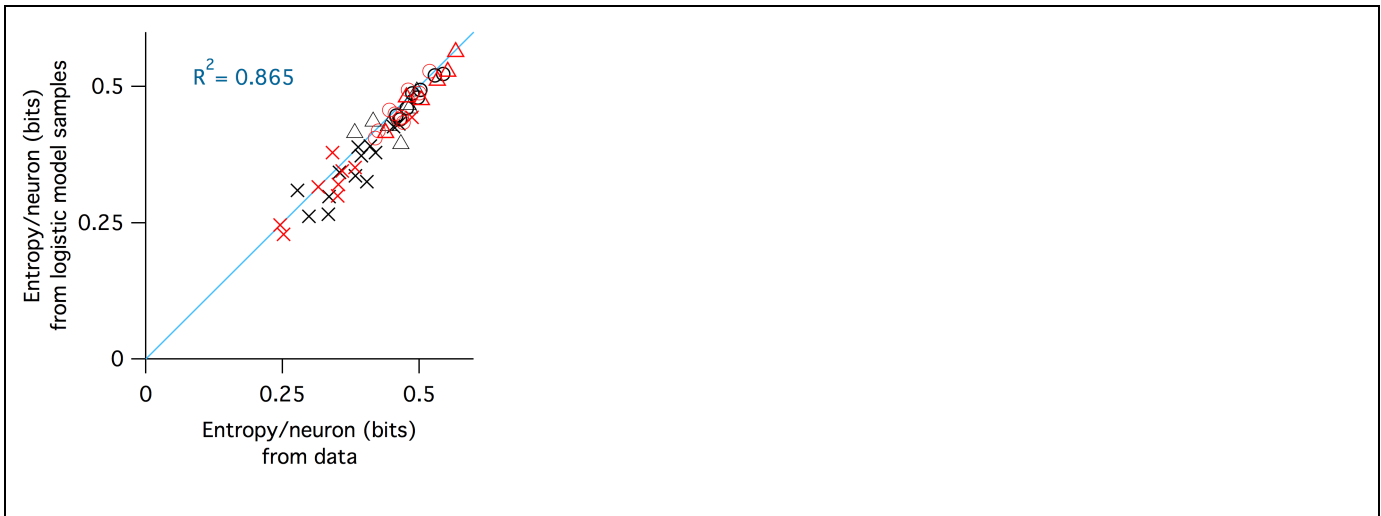


**Figure 6 – figure supplement 1. Agreement between entropy estimated from raw data with entropy estimated from samples from fitted logistic models.**

Black symbols are WT, red are *Fmr1* KO. Crosses are P9–11, circles P14–16, triangles P30–40. Blue line is identity, the  $R^2$  value of which is reported in the inset.